Converging pathways direct synapse elimination through the homeodomain transcriptional regulator DVE-1

Kellianne D Alexander[1], Shankar Ramachandran[1], Christopher M Lambert[1], Julia Russell[1], Devyn B Oliver[1], William Armstrong[1], Monica Rettler[1], Maria Doitsidou[2], Claire Bénard[3], *Michael M Francis[1]

[1]Department of Neurobiology, University of Massachusetts Chan Medical School, Worcester, United States

[2]Centre for discovery brain sciences, University of Edinburgh, Edinburgh, Scotland

[3]Department of Biological Sciences, University of Quebec at Montreal, Quebec, Canada

*Corresponding author: Michael.francis@umassmed.edu

Key words:

transcription factor, DVE-1, SATB, *C. elegans*, synapse development, synapse remodeling

Contributions Summary

K.D.A. generated strains, transgenic lines, molecular constructs, confocal microscopy images and analysis, performed optogenetic behavioral experiments, photoconversion experiments, modencode ChIP-seq analysis and pathway analysis. S.R, performed all calcium imaging experiments/analysis and conducted single worm tracking. C.L. generated most vectors and constructs. J.R. assisted with generation of CRISPR/Cas9 generated strains. W.A. and M.R. assisted with aldicarb behavioral assay. D.O. assisted with EMS screen and isolation of *dve-1* mutant. C.B. and M. D. aided in CloudMap bioinformatic analysis of uf171 mutant. M.M.F. and K.D.A designed and interpreted results of all experiments and wrote the manuscript.

Competing Interests Declared: No competing interests declared

Acknowledgements

We would like to thank Dori Schafer and the members of the Francis lab for critical reading of the manuscript. We also thank Ye Tian and Cole Haynes for generously sharing reagents and Michael Gorczyca and Will Joyce for technical assistance. We would like to thank Mark Alkema and Jeremy Florman for access to Single Worm Tracking equipment and Jeremy Florman for Matlab analysis scripts. Some nematode strains were provided by the *Caenorhabditis* Genetics Center which is funded by the NIH National Center for Research Resources and the National Bioresource Project Nematode of Japan.

Funding

This research was supported by NIH NINDS RO1NS064263 (MMF), HHMI Gilliam GT11432 (KA), and IMSD T32GM135701 (KA).

Abstract

An important step in brain development is the remodeling of juvenile neural circuits to establish mature connectivity. The elimination of juvenile synapses is a critical step in this process; however, the molecular mechanisms directing synapse elimination processes and their timing are not fully understood. We identify here a conserved transcriptional regulator, DVE-1, that directs the elimination of juvenile synaptic inputs onto remodeling *C. elegans* GABAergic neurons. Dorsally localized juvenile acetylcholine receptor clusters and apposing presynaptic sites are eliminated during maturation of wild type GABAergic neurons but persist into adulthood in *dve-1* mutants. The persistence of juvenile synapses in *dve-1* mutants does not impede synaptic growth during GABAergic remodeling and therefore results in heightened motor connectivity, producing a turning bias during movement. DVE-1 is localized to GABAergic nuclei prior to remodeling and DVE-1 nuclear localization is required for synapse elimination to proceed. Synaptic remodeling is antagonized by the expression of the Ig domain protein OIG-1. Premature synapse elimination in *oig-1* mutants is reversed by *dve-1* mutation, while precocious synaptic growth is unaffected, indicating a functional separation of synapse destruction and growth during remodeling. Together, our findings demonstrate a novel strategy for sculpting mature connectivity through the coordination of parallel DVE-1-regulated pro-degenerative processes and temporally regulated maintenance mechanisms.

Introduction

The mature human brain is composed of billions of neurons that are organized into functional circuits based on stereotyped patterns of synaptic connections that optimize circuit performance. Mature circuit connectivity is choreographed through a remarkable period of developmental circuit rewiring that is broadly conserved across species [1-5]. During this rewiring or remodeling phase, the mature circuitry is established through a tightly controlled balance: on the one hand, degenerative processes promote the elimination of juvenile synapses, while, on the other hand, maintenance or growth processes support the stabilization or formation of new connections. A combination of cell-intrinsic and extrinsic factors shape the progression of these events. For instance, activity-dependent microglial engulfment and elimination of synaptic material shapes connectivity of the retinogeniculate system in mice [6-9], while cell-intrinsic genetic programs such as the circadian clock genes Clock or Bmal1 influence GABAergic maturation and plasticity-related changes in the neocortex [10]. While molecular mechanisms supporting axon guidance and synapse formation have received considerable attention, our understanding of neuron-intrinsic molecular mechanisms controlling synapse elimination remains more limited. In particular, it is unclear how neuron-intrinsic synapse elimination processes are engaged and regulated spatiotemporally in developing neural circuits. Improved mechanistic knowledge of these processes offers potential for important advances in our grasp of both brain development and the pathology underlying numerous neurodevelopmental diseases associated with altered connectivity and neurodegenerative diseases where synapse loss is a hallmark feature [11-15]. Indeed, recent work has suggested intriguing parallels between the elimination of synapses during development and neurodegenerative processes during disease [2, 12, 14, 16].

The nematode *Caenorhabditis elegans* offers significant assets for addressing mechanistic questions about developmental neural circuit remodeling, in particular, the control of synapse elimination. *C. elegans* progresses through a highly stereotyped period of nervous system remodeling that establishes the neural connections characteristic of mature animals. 80 of the 302 neurons composing the adult nervous system, including 52 motor neurons, are born and integrated into pre-existing juvenile circuits following the first larval stage (L1) of development [17, 18]. The incorporation of these post-embryonically born motor neurons is accomplished through a remarkable reorganization of circuit connectivity. One of the most striking aspects of this reorganization is the remodeling of synaptic connections in the GABAergic dorsal D-class (DD) motor neurons (**Figure 1A**) [19-21]. Immediately after hatch, juvenile cholinergic synaptic contacts onto GABAergic DD neurons are located dorsally, while juvenile DD synaptic outputs onto muscles are located ventrally. During remodeling, dorsal cholinergic synaptic inputs to DD neurons formed in the embryo are eliminated, and new synaptic contacts from post-embryonic-born presynaptic cholinergic neurons are established ventrally. In parallel, ventral DD GABAergic synaptic terminals are relocated dorsally, forming new GABAergic synaptic contacts onto dorsal muscles [22-27]. Though we now have a growing appreciation of the cellular processes that direct the redistribution of DD GABAergic synaptic terminals, we have a limited understanding of how cholinergic synaptic contacts onto DD neurons are remodeled. Prior work suggested a mechanism for antagonizing the remodeling of cholinergic inputs to DD neurons through temporally controlled expression of the Ig domain family member OIG-1 [28, 29]; however, the mechanisms that promote remodeling of these inputs, in particular their elimination, have remained uncharacterized.

We report the identification of a mechanism for a neuron-intrinsic transcriptional control of synapse elimination during remodeling of the *C. elegans* motor circuit. From a forward genetic

screen to isolate mutants where juvenile postsynaptic sites on GABAergic DD neurons persist in mature animals, we obtained a mutation in the homeodomain transcriptional regulator *dve-1* that shares homology with mammalian special AT-rich sequence-binding (SATB) family members. We show that DVE-1 acts cell autonomously in GABAergic DD neurons to support the removal of juvenile cholinergic synaptic inputs. Juvenile synaptic inputs are maintained into adulthood in *dve-1* mutants, leading to an accumulation of presynaptic cholinergic vesicles as well as alterations in circuit function and movement. We further show that precocious synapse elimination in *oig-1* mutants is reversed by mutation of *dve-1*, suggesting that DVE-1 supports pro-degenerative processes that are antagonized by OIG-1. Our results reveal a novel neuron-intrinsic mechanism for temporally controlling synapse elimination through converging pro-degenerative and maintenance pathways.

Results

Distinct mechanisms direct developmental remodeling of presynaptic terminals versus postsynaptic sites in GABAergic neurons

Previous work by our lab and others showed that clusters of postsynaptic ionotropic acetylcholine receptors (iAChR) denote postsynaptic sites onto DD neurons and undergo dorsoventral remodeling during the transition between the 1st and 2nd larval stages of development (L1/L2 transition) [28-30]. During this period, dorsal postsynaptic sites on DD neurons are removed, and the growth of new ventral postsynaptic sites is indicated by the appearance of newly formed ventral iAChR clusters. In animals co-expressing the synaptic vesicle marker mCherry::RAB-3 and the iAChR marker ACR-12::GFP, we found that the remodeling of cholinergic postsynaptic sites and GABAergic presynaptic terminals in DD neurons occurred with similar time courses, consistent with prior work (**Figure S1.1A, B**). Surprisingly, however, we found that mutations in several genes previously implicated in the remodeling of GABAergic presynaptic terminals had no appreciable effect on the remodeling of cholinergic postsynaptic sites in DD neurons (**Figure S1.1C, Table 1**). For example, juvenile mCherry::RAB-3 clusters remained present in the ventral nerve cord of *ced-3/*caspase mutants at the L4 stage, indicating a failure to properly relocate GABAergic presynaptic terminals during remodeling. However, juvenile cholinergic postsynaptic sites were properly removed in DD neurons of *ced-3* mutants, as indicated by the absence of iAChR clusters in the dorsal nerve cord after the L2 stage (**Figure S1.1C**). Indeed, lingering synaptic vesicle clusters in the ventral nerve cord of *ced-3* mutants were interleaved with newly formed ventral iAChR clusters, demonstrating that the formation of new ventral postsynaptic sites during remodeling also occurs independently of *ced-3*. Surprisingly, mutations in several genes important for neurotransmitter release and calcium signaling also did not appreciably alter the remodeling of postsynaptic sites in DD neurons, though we noted clear delays in the remodeling of DD presynaptic terminals as found previously [25, 26] (**Table 2**). Of the genes we tested, only

mutation of the RyR/*unc-68* gene produced a modest delay in the remodeling of postsynaptic sites, perhaps suggesting a contribution of calcium release from intracellular stores (**Table 2**). Taken together, our findings demonstrate that mechanisms for the remodeling of postsynaptic sites in DD neurons are distinct from those previously implicated in the remodeling of DD GABAergic presynaptic terminals.

Identification of *dve-1* as a novel transcriptional regulator of synapse elimination

Motivated by these findings, we pursued a forward genetic strategy to identify novel mechanisms controlling the remodeling of postsynaptic sites in DD neurons. We screened to obtain mutants where juvenile postsynaptic sites, indicated by dorsal iAChR clusters, were not properly eliminated during remodeling and instead persisted into maturity (**Figure S1.2A, B**). We isolated a recessive mutant, *uf171*. Dorsal postsynaptic sites are normally eliminated before the L2 stage (22 hours after hatch) in wild type but remained visible through the late L4 stage (>40 hours after hatch) in *uf171* mutants (**Figure 1B, C, E, Figure S1.3A**). Whole genome sequence analysis of *uf171* mutants revealed a point mutation in the gene encoding the homeodomain protein DVE-1, producing a proline to serine (P/S) substitution (**Figure 1D**). Expression of the wild type *dve-1* gene in *dve-1(uf171)* mutants restored normal elimination of juvenile postsynaptic sites (**Figure 1B, C; Figure S1.3A),** while *dve-1* overexpression in wild type animals did not produce appreciable changes in removal (**Figure 1B, C; Figure S1.3A**). A similar failure in the elimination of juvenile postsynaptic sites was also evident in another available *dve-1* mutant, *dve-1(tm4803)*, that harbors a small insertion/deletion mutation (**Figure 1 B, C, Figure S1.3 A**). DVE-1 was of particular interest as it is a homeodomain transcription factor sharing homology with mammalian SATB transcription factors and was previously implicated in the regulation of a mitochondrial stress response in *C. elegans* [31]. The P/S substitution encoded by *dve-1(uf171)* affects a highly

conserved proline residue predicted to lie within a loop between helices I and II of the first homeobox domain of *dve-1*. *dve-1(tm4803)* deletes a portion of predicted helix III in the same homeobox domain, as well as a splice site leading to 65 bp insertion (**Figure 1 D**) [32, 33]. As *dve-1* null mutants are embryonic lethal [31], both mutations are predicted to be hypomorphic.

The postsynaptic scaffold protein LEV-10 is associated with cholinergic postsynaptic sites in body wall muscles and GABAergic neurons [34, 35]. Using a previously developed strategy for cell-specific labeling of endogenous LEV-10 [35], we found that mutation of *dve-1* also slowed the removal of LEV-10 from the dorsal processes of DD neurons during remodeling. LEV-10 was primarily associated with dorsal processes prior to remodeling and was redistributed to ventral processes during remodeling (**Figure 1F**). Similar to juvenile iAChR clusters, dorsal LEV-10 scaffolds in GABAergic neurons of *dve-1* mutants were not properly eliminated during remodeling, further demonstrating that DVE-1 coordinates the removal of juvenile postsynaptic sites in DD neurons. Interestingly, mutation of *dve-1* did not affect the formation of new ventral postsynaptic sites on DD neurons during remodeling or their abundance (**Figure 1E, G Figure S1.3B**). Likewise, mutation of *dve-1* had little effect on the density of DD dendritic spines that are formed after remodeling (**Figure S1.3C, D**) [36-38]. These findings indicate that the evolutionarily conserved transcription factor DVE-1 specifically governs the elimination of juvenile postsynaptic sites during remodeling without affecting the formation or maturation of new postsynaptic sites. Notably, the remodeling of DD GABAergic presynaptic terminals also occurred normally in *dve-1* mutants (**Figure 1G**), further supporting that distinct neuron-intrinsic programs direct remodeling of the pre- and postsynaptic domains of GABAergic DD neurons (**Figure 1G; Figure S1.1C; Tables 1, 2**).

Lingering iAChRs in *dve-1* mutants are organized into structural synapses

To test if lingering juvenile postsynaptic sites in the dorsal nerve cord of *dve-1* mutants are organized into structurally intact synapses, we first asked whether these iAChR clusters were localized at the cell surface. Using an approach for *in vivo* antibody labeling of cell surface receptors [38, 39], we found that lingering iAChR clusters were visible in the dorsal cord of *dve-1* mutants, but not in controls (**Figure 2A**). We also found that most iAChR clusters retained in dorsal GABAergic DD processes of *dve-1* mutants were closely apposed by synaptic vesicle assemblies of cholinergic DA/B axons in the dorsal nerve cord (**Figure 2B**). During remodeling, DA/B connections with DD neurons in the dorsal nerve cord are removed and new connections are established between DA/B motor neurons and post-embryonic born ventrally directed VD GABAergic motor neurons (**Figure 1A, Figure 2C**). To investigate the remodeling of cholinergic terminals in axons presynaptic to DD neurons, we expressed the photoconvertible synaptic vesicle marker Dendra2::RAB-3 in cholinergic DA/B neurons (**Figure 2D**). We first examined the distribution of Dendra2::RAB-3 in the wild type dorsal nerve cord immediately prior to the onset of DD remodeling (approximately 14 hours after hatch) (**Figure 2E**). Prior to photoconversion, clusters of green Dendra2::RAB-3 fluorescence were distributed along the length of cholinergic axons in the dorsal nerve cord. Brief exposure of the dorsal nerve cord to 405 nm light produced immediate and irreversible photoconversion of Dendra2::RAB-3 signals from green to red fluorescence (**Figure S2.1E**). In wild type, Dendra2::RAB-3 clusters that had been photoconverted to red fluorescence prior to the onset of remodeling were strikingly reduced following remodeling (10 hours later, 55 ± 9% reduction) and were replaced by new synaptic vesicle clusters (green fluorescence) (**Figure 2E, F; Figure S2.1A, B, E**). In contrast, wild type Dendra2::RAB-3 clusters photoconverted after completion of remodeling (at approximately 24 hours after hatch) remained largely stable over the subsequent 10 hours (**Figure 2G-H**, **Figure S2.1F**). We also noted the appearance of green RAB-3 clusters during this time frame (24-34 hours after hatch), indicating parallel addition of new vesicular material (**Figure S2.1C, D, F**).

Thus, synaptic vesicle clusters in wild type DA/B axons are largely removed and replaced during the 10-hour period of remodeling but are more stable over a 10-hour time window immediately following completion of remodeling, offering intriguing evidence for developmental stage-specific regulation of cholinergic synaptic vesicle stability. Importantly, this transient reorganization of presynaptic release sites in wild type cholinergic axons occurs concurrently with the removal and remodeling of postsynaptic sites in DD GABAergic neurons.

We noted a striking change in the stability of synaptic vesicle material in cholinergic axons of *dve-1* mutants during remodeling. Dorsal cholinergic Dendra2::RAB-3 clusters photoconverted prior to the onset of synaptic remodeling were preserved throughout remodeling in *dve-1* mutants (**Figure 2E,F, Figure S2.1E**), indicating enhanced stability of cholinergic terminals presynaptic to DD neurons. The addition of new synaptic vesicles during this time frame (14-24 hours after hatch) was not appreciably affected by mutation of *dve-1*, as indicated by similar increases in green Dendra2::RAB-3 fluorescence across wild type and *dve-1* mutant cholinergic axons (**Figure S2.1A, B, E**). RAB-3 clusters that were photoconverted after the completion of remodeling (approximately 24 hours after hatch) remained detectable 10 hours later in *dve-1* mutants, also similar to wild type (**Figure 2G, H; Figure S2.1F**). Dorsal axon green Dendra2::RAB-3 fluorescence was increased by roughly 2-fold in *dve-1* mutants compared to wild type 24-34 hours after hatch, suggesting enhanced addition or stabilization of new synaptic vesicles at *dve-1* mutant cholinergic axon terminals after remodeling (**Figure S2.1C, D, F**). To explore this in more detail, we examined the distribution of the synaptic vesicle marker SNB-1::GFP in dorsal cholinergic axons of L4 stage *dve-1* mutants. The intensity of SNB-1::GFP clusters was increased in dorsal cholinergic axons of *dve-1* mutants compared to wild type (**Figure 2I**), whereas SNB-1::GFP fluorescence intensity in ventral cholinergic axons of *dve-1* mutants was unchanged (**Figure 2J**), suggesting specificity of DVE-1 actions for cholinergic synaptic contacts onto DD

neurons (**Figure S2.1E**). Notably, UNC-10::GFP fluorescence intensity (labeling active zones) in L4 stage dorsal cholinergic axons was not appreciably affected by *dve-1* mutation (**Figure S2.1E**). Thus, mutation of *dve-1* leads to an increase in the stability or recruitment of synaptic vesicle material at dorsal cholinergic axon terminals but does not appreciably alter the size or density of active zones. Overall, our results indicate that *dve-1* promotes destabilization of both cholinergic postsynaptic sites in GABAergic neurons and presynaptic cholinergic vesicle assemblies during remodeling.

A failure to eliminate postsynaptic sites via DVE-1 leads to enhanced activity and altered motor behavior

To investigate how a failure of synapse elimination may impact circuit function, we first sought to determine whether preserved structural connections between dorsal cholinergic axons and GABAergic DD neurons of *dve-1* mutants were functional in adults. To address this question, we used combined cell-specific expression of Chrimson for cholinergic depolarization [40, 41] and GCaMP6 for monitoring [Ca^{2+}] changes in the postsynaptic GABAergic motor neurons [42] (**Figure S3.1A**). We recorded Ca^{2+} transients from young adult GABAergic DD or VD motor neurons in response to presynaptic DA/B cholinergic depolarization. We did not observe an appreciable change in the magnitude of stimulus-elicited Ca^{2+} transients in VD neurons but noted striking changes in DD neurons. Specifically, we found that photostimulation elicited a modest Ca^{2+} response in roughly 37% of wild type DD neurons tested, consistent with a low degree of synaptic connectivity between these neurons in adults as predicted by the wiring diagram [18, 43]. The percentage of responsive DD neurons (85%) and the average magnitude of stimulus-elicited Ca^{2+} transients increased significantly for *dve-1* mutants (**Figure 3A**), demonstrating

enhanced functional connectivity between dorsal cholinergic neurons and GABAergic DD neurons of adult *dve-1* mutants.

We next asked how altered functional connectivity in the motor circuit of *dve-1(uf171)* mutants might affect circuit performance and behavior. Automated tracking of single worms during exploratory behavior showed *dve-1(uf171)* mutants frequently moved in loose, dorsally directed circles, whereas wild type animals were more likely to adopt straight trajectories (**Figure 3B**). During 5 minutes of continuous tracking, roughly 80% of *dve-1(uf171)* mutants circled, approximately 60% of these in the dorsal direction, while only 20% of wild type circled (**Figure 3B, C**). The dorsal circling behavior of *dve-1* mutants suggested that altered synaptic output from the motor circuit may produce a turning bias. In addition to GABAergic neurons, dorsally directed DA/B cholinergic motor neurons are presynaptic to body wall muscles. We speculated that the increased abundance of cholinergic synaptic vesicles in dorsal motor axons of *dve-1* mutants may enhance dorsal cholinergic transmission onto muscles and elicit more robust dorsal turning. In support of this idea, we found that *dve-1* mutants were hypersensitive to the paralyzing effects of the acetylcholinesterase inhibitor aldicarb, an indicator of elevated acetylcholine release [44] (**Figure S3.1B**).

To explore this idea further, we tracked animals during depolarization of dorsal cholinergic neurons by cell-specific photoactivation using Chrimson. Prior to stimulation, control animals moved in long forward trajectories (**Figure 3D-F**). As expected, photostimulation of DA/B motor neurons (625 nm, 14 mW/cm^2) increased dorsal turning by ~2.5 fold in control animals, often leading to large dorsally oriented circles (**Figure 3D, G**). By comparison, photostimulation of *dve-1* mutant DA/B motor neurons strikingly increased dorsal turning, leading to tight dorsally oriented

circles (**Figure 3D-H**). The enhanced dorsal turning of *dve-1* mutants was associated with an increase in the depth of dorsal bends compared to wild type (**Figure 3G, H, Figure S3.1 C, D**) and was not observed in animals that lacked Chrimson expression or in the absence of retinal chromophore (**Figure S3.1E, F**). Chrimson expression was also not appreciably different across *dve-1* mutants and controls (**Figure S3.1G**). We propose that increased acetylcholine release onto dorsal muscles of *dve-1* mutants enhances dorsal bending and circling, perhaps due to an increase in the size of the synaptic vesicle pool in dorsal cholinergic axons. This interpretation is consistent with the increased abundance of synaptic vesicle material in dorsally projecting cholinergic axons of *dve-1* mutants. Ectopic activation of dorsally projecting GABAergic DD neurons in *dve-1* mutants might be expected to enhance dorsal inhibition, countering the effects of dorsal excitation. However, we speculate that the number and strength of synaptic connections from dorsal cholinergic motor neurons to dorsal body wall muscles overwhelms any increase in dorsal inhibition. Together, our results suggest mutation of *dve-1* impacts functional connectivity both through retention of juvenile connectivity onto DD motor neurons and through an increase in cholinergic transmission onto dorsal muscles.

DVE-1 localization to GABAergic nuclei is required for synapse elimination

To better understand potential mechanisms for DVE-1 actions in synapse elimination, we examined *dve-1* expression using a strain where a GFP coding sequence was inserted in the *dve-1* genomic locus [45]. As noted previously [45], we observed prominent DVE-1::GFP expression in intestinal cells. However, we also observed neuronal expression of endogenously labeled DVE-1::GFP in roughly 20 neurons at the L1 stage prior to remodeling [46]. Notably, in the ventral nerve cord DVE-1 was solely expressed in DD GABAergic neurons (**Figure 4A, B**). Further, DVE-1 was specifically localized to GABAergic nuclei, where it is assembled in discrete nuclear foci during

the time frame of synaptic remodeling. Similar nuclear DVE-1 clusters have been observed in intestinal cell nuclei where DVE-1 is thought to associate with loose regions of chromatin and organize chromatin loops in order to regulate gene expression during mtUPR [45]. We found that DVE-1::GFP expression in GABAergic neurons requires the Pitx family homeodomain transcription factor UNC-30, the terminal selector of *C. elegans* GABAergic motor neuron identity (**Figure S4.1A**) [47-49]. Consistent with this, putative UNC-30 binding sites [47-49] are present within the DVE-1 promoter region. In contrast, mutation of *unc-30* produced no appreciable change in DVE-1::GFP fluorescence in intestinal cells, indicating cell type-specific mechanisms for regulation of *dve-1* expression (**Figure S4.1B**).

Prior studies of DVE-1 in intestinal cells showed that deSUMOylation of DVE-1, mediated by the isopeptidase ULP-4, is required for its nuclear localization [50]. To explore whether DVE-1 localization to DD GABAergic nuclei might be important for DVE-1 regulation of synapse elimination, we asked if the nuclear localization of DVE-1 in GABAergic neurons is also regulated by ULP-4. We observed that mutation of *ulp-4* caused a striking decrease of *dve-1::*GFP fluorescence in GABAergic neuron nuclei and eliminated *dve-1::*GFP nuclear foci (**Figure 4B, C**). A mutated form of DVE-1, DVE-1K327R, where a key lysine residue required for SUMOylation is mutated to arginine [50], localized to GABAergic nuclei in the absence of *ulp-4* (**Figure 4B, C**), demonstrating specificity. The elimination of dorsal iAChR clusters during remodeling was strikingly disrupted by mutation of *ulp-4*, such that dorsal iAChR clusters remain present in roughly 50% of L4 stage animals (**Figure 4 D-F**). Either pan-neuronal or GABA neuron-specific expression of the wild type *ulp-4* gene in *ulp-4* mutants was sufficient to restore the elimination of dorsal iAChRs, while intestinal *ulp-4* expression was not (**Figure 4 D-F**). We conclude that the localization of DVE-1 to GABAergic nuclei is essential for synapse elimination during remodeling, and this localization is regulated at least in part by SUMOylation. Notably, the nuclear localization

of mammalian SATB family members is also dependent on SUMOylation, indicating conserved regulatory mechanisms [51, 52].

Analysis of DVE-1 transcriptional targets reveals several pathways with relevance for synapse elimination

Recent work revealed that homeodomain transcription factors are broadly utilized in the specification of *C. elegans* neuronal identity [46]. Given its homology to mammalian SATB family transcription factors, we asked whether DVE-1 transcriptional regulation may be important for GABAergic neuronal identity. We found that the numbers of DD neurons and commissures were unchanged in *dve-1* mutants compared to wild type (**Figure S5.1 A**). In addition, we found that the expression levels of three GABAergic markers in DD neurons (*unc-47*/GABA vesicular transporter, *unc-25*/glutamic acid decarboxylase, and *flp-13*/FMRFamide neuropeptide) were not appreciably altered by *dve-1* mutation (**Figure S5.1B**). These results support that DVE-1 is not critical for GABAergic identity of the DD neurons but instead may regulate other aspects of GABAergic neuron development, such as the transcription of effectors important for synapse elimination.

To reveal potential direct targets of DVE-1 in GABAergic neurons, we analyzed chromatin immunoprecipitation followed by sequencing (ChIP-Seq) data available from the modENCODE consortium [53]. We found 1044 genes with strong DVE-1 binding signal in their promoter regions, implicating these genes as potential direct targets of DVE-1 transcriptional regulation (**File S5**). We noted that 627 of these had significant expression in GABAergic neurons based on available single-cell RNA-seq data (**File S5**) [54, 55]. Pathway analysis of the GABAergic neuron-enriched targets using WormCat [56] and WormenrichR [57, 58] revealed a significant enrichment of genes

involved in the mitochondrial unfolded protein response (mtUPR) stress pathway (**Figure 5A, File S5)**, as expected from prior studies [31, 50, 59]. Notably, our analysis also revealed enrichment of genes involved in ribosomal composition, endocytic and phagocytotic function, the ubiquitin-proteasome system, as well as various signaling pathways (**Figure 5A; Figure S5.2 E, File S5**).

DVE-1-dependent synapse elimination occurs independently of mtUPR

To clarify which of the pathways identified from our analysis may be most critical, we next asked whether activation or inhibition of mtUPR impacted synapse elimination. We first quantified the length and density of mitochondria in DD neurons and found no differences between wild type and *dve-1* mutants (**Figure S5.2A**). We next measured mtUPR activation in *dve-1* mutants by quantifying *hsp-6pr::*GFP fluorescence [31]. Surprisingly, we noted increased levels of intestinal *hsp-6pr::*GFP expression in *dve-1* mutants compared with control, suggesting elevated mtUPR activity (**Figure S5.2B, C**). The transcription factor ATFS-1 is required for the *hsp-6pr::*GFP transcriptional response and activation of the mtUPR [60]. Knockdown of *atfs-1* by feeding RNAi decreased *hsp-6pr::*GFP signal in *dve-1* mutants (**Figure S5.2C**), indicating reduced mtUPR activation following *atfs-1* knockdown. However, *atfs-1* knockdown failed to restore normal removal of dorsal iAChR clusters in *dve-1* mutants (**Figure S5.2D**). Likewise, a null mutation in *atfs-1* did not alter synapse elimination in single mutants and failed to restore synapse elimination in *atfs-1;dve-1* double mutants (**Figure 5B**). These results show that increased activation of the mtUPR in *dve-1* mutants is not sufficient to account for a failure in synapse removal. Consistent with this interpretation, constitutive mtUPR activation by mutation of the mitochondrial complex III subunit gene *isp-1* also did not alter synapse elimination (**Figure 5B**) [61]. Additionally, mutation of *ubl-5*, a cofactor with DVE-1 in the initiation of the mtUPR [62], did not affect synapse elimination (**Figure 5B**). Our findings demonstrate that mtUPR activation or inhibition does not

alter synapse removal. We conclude that DVE-1 coordinates synapse elimination through transcriptional regulation of alternate pathways identified from our enrichment analysis, such as those governing protein expression (ribosome composition/ubiquitin-proteasome pathway) or homeostasis (endocytic/phagocytic function) (**Figure 5A, Figure S5.2E**).

Synapse elimination occurs through a convergence of DVE-1 regulated destabilization and removal of OIG-1 antagonism

The timing of DD neuron remodeling is, in part, determined through temporally controlled expression of the Ig-domain protein OIG-1 [29, 38]. The expression of an *oig-1pr::*GFP transcriptional reporter in L1 stage DD neurons was not appreciably altered in *dve-1* mutants (**Figure 6A**), supporting prior evidence that *oig-1* expression is regulated independently of *dve-1*. The Ig domain protein OIG-1 normally functions to antagonize synaptic remodeling. *oig-1* mutation leads to precocious remodeling of postsynaptic sites in DD neurons, where both elimination of dorsal juvenile postsynaptic sites and formation of new ventral postsynaptic sites occur prematurely compared with wild type [29, 38]. However, unlike the precocious removal of postsynaptic sites in DD neurons of *oig-1* single mutants, we noted a striking delay in the removal of postsynaptic sites in *oig-1*;*dve-1* double mutants. Juvenile postsynaptic sites were retained in DD neurons through late L4 stage, similar to *dve-1* single mutants (**Figure 6B-C, F**). A requirement for DVE-1 in synapse elimination is therefore maintained even when antagonistic processes promoting synapse stabilization are also disrupted. Conversely, the formation of new ventral postsynaptic sites occurred precociously in DD neurons of *oig-1*;*dve-1* double mutants, similar to *oig-1* single mutants (**Figure 6D-E, F**). Thus, disruption of *dve-1* function reversed precocious synapse elimination in *oig-1* mutants but did not impact the premature assembly of ventral postsynaptic sites, supporting the independence of programs supporting synapse

elimination versus growth and suggesting independent functions for OIG-1 in each (**Figure 6F,G**). Overall, our findings show that mature connectivity is sculpted through a convergence of DVE-1 regulated elimination processes and temporally regulated OIG-1 based stabilization mechanisms.

Discussion

Developmental remodeling of synaptic connectivity occurs throughout phylogeny, refining and reorganizing neuronal connections toward the establishment of the mature nervous system. While neuron-extrinsic events that shape remodeling, for example, microglial phagocytosis of synaptic material [6-9], have gained a lot of recent attention, neuron-intrinsic processes governing remodeling have remained less well-described. Likewise, the relationship between degenerative and growth processes during remodeling have not been clearly elucidated. The developmental remodeling of *C. elegans* GABAergic DD neurons presents a uniquely accessible system for addressing important questions about evolutionarily conserved neuron-intrinsic mechanisms of remodeling because the reorganization of their connectivity occurs without gross morphological changes or a requirement for synaptic removal by other cell types.

Here, we show that the homeodomain transcription factor *dve-1* with homology to the SATB family of transcription factors is specifically required for the elimination of juvenile synaptic inputs to DD neurons during remodeling. In *dve-1* mutants, juvenile postsynaptic sites and apposing cholinergic presynaptic terminals are preserved into adulthood. The failure to eliminate these sites results in elevated activity at these synapses and impaired motor function. Interestingly, *dve-1* is not required for the growth of new DD neuron synaptic inputs that are characteristic of the mature motor circuit, indicating that the formation of new connections is not dependent upon elimination of pre-existing juvenile synapses. Likewise, mutation of *dve-1* does not alter developmental reorganization of synaptic outputs from DD neurons onto muscles. In *dve-1* mutants, newly relocated GABAergic synaptic terminals occupy similar territories in DD neurons as lingering juvenile synaptic inputs. Thus, the formation of new GABAergic presynaptic terminals during maturation of the circuit is not contingent on elimination of nearby juvenile postsynaptic sites in DD neurons.

Our findings lead us to propose that cell-autonomous transcriptional regulation of GABAergic neurons by DVE-1 promotes the elimination of their juvenile synaptic inputs. We found that DVE-1 is expressed in a limited number of neurons, including GABAergic motor neurons, and DVE-1 localization to GABAergic nuclei is required for synapse elimination to proceed normally. DVE-1 regulation of synapse elimination shares interesting parallels with a previously described pathway for elimination of postsynaptic structures at mouse glutamatergic synapses through transcriptional regulation by Myocyte Enhancer Factor 2 (Mef2) [63-65]. However, in contrast to MEF2-regulated synapse elimination, we found that DVE-1 regulated elimination of synapses to DD neurons is not strongly activity-dependent. Also, we did not observe strong temporal regulation of DVE-1 expression in GABAergic neurons prior to or during remodeling. These observations raise important questions about temporal control of synapse elimination. One possible route for temporal regulation might be through control of DVE-1 nuclear localization. We show that DVE-1 localization to GABAergic nuclei can be regulated through SUMOylation. However, we observed nuclear localization of DVE-1 in GABAergic neurons prior to the onset of remodeling, suggesting the presence of additional mechanisms for temporal control. This is consistent with prior work indicating that temporally controlled expression of OIG-1 regulates the timing of remodeling [28]. We found that precocious synapse elimination in *oig-1* mutants is reversed when *dve-1* function is also disrupted, further indicating that DVE-1 transcriptional regulation is required for synapse elimination to occur. In contrast, precocious growth of new synapses in *oig-1* mutants was not altered by mutation of *dve-1*, suggesting a hierarchical organization of remodeling processes where DVE-1 regulated degenerative mechanisms act in parallel with growth processes that are regulated independently (**Figure 5 F-G**).

Our experiments show that mutation of *dve-1* affects the stability of both postsynaptic sites in DD GABAergic neurons and presynaptic terminals in cholinergic neurons. We show that the juvenile

synaptic vesicle assemblies in axons of presynaptic cholinergic neurons are almost completely exchanged during the 10-hour period of wild type remodeling. This turnover of synaptic vesicles during remodeling contrasts with the relative stability of wild type synaptic vesicles over the 10 hours immediately following remodeling. Thus, turnover of synapse-associated vesicles in presynaptic cholinergic axons occurs at a higher rate during circuit rewiring, suggesting temporal regulation of an active process for presynaptic reorganization. Notably, removal of juvenile synaptic vesicle assemblies during remodeling is strikingly reduced in *dve-1* mutants, indicating that disruption of DVE-1 transcriptional activation is sufficient to stabilize presynaptic vesicle pools in cholinergic neurons. Since DVE-1 is solely expressed in postsynaptic GABAergic neurons, our results suggest that DVE-1-regulated postsynaptic pathways promote exchange or elimination of juvenile presynaptic elements through destabilization of the postsynaptic apparatus. Our photoconversion experiments also show that recruitment of new synaptic vesicles in cholinergic axons of *dve-1* mutants is not halted by the stabilization of juvenile synaptic vesicle assemblies. Consistent with this, we noted an overall increase in dorsal synaptic vesicle material in *dve-1* mutants compared with either wild type or ventral synapses of *dve-1* mutants. Our Ca^{2+} imaging and behavioral experiments provide evidence that the increase in cholinergic synaptic vesicles of dorsally projecting motor neurons alters circuit function such that cholinergic activation of dorsal musculature is enhanced in *dve-1* mutants, resulting in deeper dorsal bends and a dorsal turning bias during movement.

The closest homolog of DVE-1 is the *Drosophila* homeodomain transcription factor *defective proventriculus* (*Dve*). Interestingly, transcriptional profiling of *Drosophila* mushroom body gamma neurons during remodeling showed Dve expression peaks at the onset of remodeling [66]. DVE-1 also shares homology with the mammalian chromatin organizers special AT-rich sequence-binding (SATB) proteins 1 and 2. In the context of the mtUPR, DVE-1/SATB is thought to organize loose chromatin to induce expression of chaperones and proteases [31, 59, 62]. Indeed, our

pathway analysis of DVE-1 ChIP-seq data showed a high enrichment of genes involved in the mtUPR. However, manipulations that either activated or inhibited the mtUPR did not affect remodeling, providing support for a model where DVE-1 regulation of remodeling is distinct from DVE-1 function in mtUPR. In addition to the mtUPR, our analysis of DVE-1 targets revealed enrichment of genes in other pathways that may represent alternative targets of DVE-1 for removal of synapses, for example, through regulation of protein expression (ribosome/ER processing) or engulfment (endocytosis/phagocytosis). The SATB family of transcriptional regulators have been shown to play roles in many areas of mammalian brain development, such as the activation of immediate early genes important for maintaining dendritic spines in GABAergic interneurons [67] and cortex development and maturation [68, 69], but roles in synapse elimination had been previously uncharacterized. Our findings offer a striking example of DVE-1/SATB transcriptional activation of pro-degenerative pathways acting in concert with temporally controlled expression of a maintenance factor to control a developmentally defined period of synapse elimination. Given the conservation of DVE-1 and the mammalian SATB family of transcriptional regulators, our analysis may shed light on new mechanisms by which SATB family transcription factors control brain development. Importantly, dysfunction of these transcription factors in humans, as in SATB2-associated syndrome, is characterized by significant neurodevelopmental delays, limitations in speech, and severe intellectual disability [70-72]. More broadly, our findings highlight a cellular strategy for temporal control of circuit development through convergent regulation of antagonistic cellular processes. Interestingly, spatiotemporal regulation by competing parallel transcriptional programs is utilized in other developmental contexts across different species, suggesting this may represent a broadly utilized mechanism for temporal control of key developmental events [73-77].

Materials and Methods

Strains and Genetics

All strains are derivatives of the N2 Bristol strain (wild type) and maintained under standard conditions at 20-25°C on nematode growth media plates (NGM) seeded with *E. coli* strain OP50. Some strains were provided by the *Caenorhabditis* Genetics Center, which is funded by NIH Office of Research Infrastructure Programs (P40 OD010440), and by the National BioResource Project which is funded by the Japanese government. Transgenic strains were generated by microinjection of plasmids or PCR products into the gonad of young hermaphrodites [78]. Integrated lines were produced by X-ray irradiation or UV-integration and outcrossed to wild type/N2 Bristol. A complete list of all strains used in this work is included in supplemental file 1.

Molecular Biology

Plasmids were constructed using two-slot Gateway Cloning system (Invitrogen) and confirmed by restriction digest and/or sequencing as appropriate. All plasmids and primers used in this work are described in supplemental file 2 and 3 respectively.

To generate the DVE-1 genomic rescue the *dve-1* promoter (5 kb upstream from translational start site), genomic fragment (from translational start to stop, 6107bp), and *dve-1* 3' UTR (626bp downstream from translational stop) were amplified from genomic N2 DNA. pKA110 (*unc-129pr*::Dendra2::RAB-3) was created by ligating a gBlock (IDT) containing the Dendra2 coding sequence into NheI-HF/PstI-HF digested pDest-114 to generate pDest-339 (Dendra2::RAB-3). pDest-339 was then recombined with pENTR-*unc-129* to generate pKA110 and injected at 50 ng/µl. To generate pKA35 (*unc-129pr*::Chrimson::SL2::BFP) Chrimson was amplified from pDest-104 and ligated into NheI-HF/BstBI digested pDest-239 to generate pDest-240

(Chrimson::SL2::BFP). pDest-240 was then recombined with pENTR-*unc-129* to generate pKA35 and injected at 50 ng/µl.

To generate ULP-4 rescue constructs ULP-4 cDNA was amplified from RNA and ligated into NheI-HF/KpnI-HF digested pDest-139 to generate pDest-291(ULP-4cDNA). pDest-291 was recombined with pENTR-*unc-47* to generate pKA76 (*unc-47pr*::ULP-4cDNA), pENTR-F25B3.3 to generate pKA78 (F25B3.3pr::ULP-4cDNA), and pENTR-*gly-19* to generate pKA80 (*gly-19pr::*ULP-4cDNA). All *ulp-4* rescue constructs were injected at 30 ng/µl.

pKA74 (*unc-47pr*::NLS::mCherry) was created by amplifying an artificial intron and NLS from plasmid #68120 (Addgene) and was ligated into AgeI-HF/XbaI digested pDest-145 to generate pDest-205(NLS::mCherry). pDest-205 was recombined with pENTR-*unc-47* to generate pKA74 and injected at 50 ng/µl.

Staging time course DD remodeling

Briefly, freshly hatched larvae were transferred to seeded OP50 plates and maintained at 25°C (timepoint 0). Imaging and analysis of iAChR or synaptic vesicle remodeling was assessed as previously described [28].

Confocal imaging and analysis

Unless noted otherwise, all strains were immobilized with sodium azide (0.3M) on a 2% or 5% agarose pad. All confocal Images were obtained either using an Olympus BX51WI spinning disk confocal equipped with a 63x objective or on the Yokogawa CSU-X1-A1N spinning disk confocal system (Perkin Elmer) equipped with EM-CCD camera (Hamamatsu, C9100-50) and 63x oil

immersion objective. Analysis of synapse number and fluorescence intensity was performed using FIJI ImageJ software (open source) using defined threshold values acquired from control experiments for each fluorescent marker. Statistical analysis for all synaptic and spine analysis between two groups utilized a student's t-test; for analysis where, multiple groups were compared an ANOVA with Dunnett's multiple comparisons test was used.

Synaptic analysis: Background fluorescence was subtracted by calculating the average intensity of each image in a region outside the ROI. All ROIs were 25 μm or 30 μm in length. Quantification of the number of puncta within an ROI had a set threshold of 25-255 and the analyze particles function of ImageJ was used to quantify any particle greater than 4 pixels^2. Fluorescence intensity was quantified from the raw integrated fluorescence within the ROI. For quantification of the DD neuron synapses the ROI was defined as either the ventral region anterior to the DD1 soma or the opposing dorsal region. For quantification of the DA/DB neuron synapses the ROI was defined as either the ventral region between DB1 and DB3 or the opposing dorsal region between VB1 and VB3.

Spine/dendrite analysis: Spine number was quantified as described previously [37, 38]. Briefly, spines were counted within a 30 μm ROI anterior to the soma of DD1. Dendrite length was defined as the anterior extension from DD1 soma to the end of the ventral process.

EMS Screen

The EMS mutagenesis protocol was adapted from [79]. *flp-13pr::*ACR-12::GFP strain IZ1905 animals were treated with 25 μM ethyl methanesulfonate (EMS, Sigma). After washing, P0 mutagenized animals were recovered. F1 animals were transferred to fresh plates and 8 F2s were isolated per F1 (F2 clonal screen). The F3 progeny of ~400 F2s per round were screened. After

27 rounds of EMS, a total of 3261 haploid genomes were screened. Each isolated candidate mutant was rescreened three times to confirm the phenotype.

Variant discovery mapping and whole genome sequencing

Mutant strains were backcrossed a single time into the IZ2302 starting strain injected with *unc-122pr::*GFP co-injection marker(enabling the distinction of cross- from self-progeny). F2 animals were isolated onto separate plates and their F3 brood were screened on a confocal microscope for a remodeling phenotype. 21 independent homozygous recombinant F2 lines were thus isolated and pooled together. Worm genomic DNA was prepared for sequencing following Gentra Puregene Tissue Kit DNA purification protocol (Qiagen). Library construction and whole genome sequencing were performed by Novogene. Briefly, NEBNext DNA Library Prep Kit was used for library construction. Pair-end sequencing was performed on Illumina sequencing platform with a read length of 150 bp at each end. Reads were mapped to *C. elegans* reference genome version WS220 and analyzed using the CloudMap pipeline [80] where mismatches were compared to the parental strain as well as to the other sequenced mutants isolated from this screen [80, 81].

Injection of fluorescent antibodies for *in vivo* labeling of iAChRs

For staining of iAChRs at the cell surface, mouse monoclonal α-HA antibodies (16B12 Biolegend) coupled to Alexa594 were diluted in injection buffer (20 mM K_3PO_4, 3 mM K citrate, 2% PEG 6000, pH 7.5). Antibody was injected into the pseudocoelom of L2/L3 stage wild type or *dve-1(uf171)* animals as described previously [28, 39]. Animals were allowed to recover for six hours on seeded NGM plates. Only animals in which fluorescence was observed in coelomocytes were included in the analysis. A student's t-test was used for statistical analysis.

Photoconversion of Dendra2::RAB-3

Wild type and *dve-1(uf171)* mutant L1 animals (12-14 hours post-hatch) expressing Dendra2::RAB3 were paralyzed using 1 mM Levamisole and imaged. Dendra2::RAB-3 puncta in the DA/DB dorsal axonal process were photoconverted using a 405 nm laser at 800 ms for 30 s. Images were acquired immediately following photoconversion and again 10 hours later. Between photoconversion and next timepoint animals were rescued and allowed to recover. Both red and green fluorescent signals were quantified. A student's t-test was used for statistical analysis.

Aldicarb paralysis assays

The aldicarb assays were performed as previously described [44]. Strains were scored in parallel, with the researcher blinded to the genotype. Young adult animals (24 hours after L4) at room temperature (22–24°C) were selected (>10 per trial for at least 3 trials) and transferred to a nematode growth medium plate containing 1 mM aldicarb (ChemService). Movement was assessed every 15 minutes for 2 hours. Animals that displayed no movement when prodded (paralyzed) were noted. The percentage of paralyzed animals were calculated at each timepoint.

Calcium imaging

Transgenic animals expressing *ttr-39pr*::GCaMP6s::SL2::mCherry (GABA neurons) along with *unc-129pr*::Chrimson::SL2::BFP (DA and DB cholinergic neurons) were grown on NGM plates with OP50 containing 2.75 mM All-Trans Retinal (ATR). L4 animals (40 hours post-hatch) were staged 24 hours prior to experiments on fresh ATR OP50 NGM plates. Imaging was performed

with 1-day age adults immobilized in hydrogel [37, 82]. Animals were transferred to 7.5 µL of the hydrogel mix placed on a silanized glass slide and covered with cover slip. Hydrogel was cured using a handheld UV Transilluminator (312 nm, 3 minutes). Chrimson photoactivation (~14 mW/cm^2) was achieved using a TTL-controlled 625 nm light guide coupled LED (Mightex Systems). A 556 nm BrightLine single-edge short-pass dichroic beam splitter was positioned in the light path (Semrock) [38]. Data were acquired at 10 Hz for 15 s using Volocity software at a binning of 4x4. Analysis was performed using ImageJ. DD and VD GABA motor neuron cell bodies were identified by mCherry fluorescence and anatomically identified by position along the ventral nerve cord. Each field typically contained 1–5 GABA motor neurons. Only recordings of neurons located anterior to the vulva were included in the analysis. Photobleaching correction was performed on background subtracted images by fitting an exponential function to the data (CorrectBleach plugin, ImageJ). Pre-stimulus baseline fluorescence (F_0) was calculated as the average of the corrected background-subtracted data points in the first 4 s of the recording and the corrected fluorescence data was normalized to prestimulus baseline as $\Delta F/F_0$, where $\Delta F=F-F_0$. Peak $\Delta F/F_0$ was determined by fitting a Gaussian function to the $\Delta F/F_0$ time sequence using Multi peak 2.0 (Igor Pro, WaveMetrics). All data collected were analyzed, including failures (no response to stimulation). Peak $\Delta F/F_0$ values were calculated from recordings of >10 animals per genotype. Mean peaks ± SEM were calculated from all peak $\Delta F/F_0$ data values. For all genotypes, control animals grown in the absence of ATR were imaged.

Single worm tracking

Single worm tracking was carried out for a duration of 5 minutes, on NGM plates seeded with 50 µL of OP50 bacteria, using Worm Tracker 2 [83]. Animals were allowed to acclimate for 30 s prior to tracking. Movement features were extracted from 5 minutes of continuous locomotion tracking.

Worm tracker software version 2.0.3.1, created by Eviatar Yemini and Tadas Jucikas (Schafer lab, MRC, Cambridge, UK), was used to analyze movement [84]. Locomotion paths were extracted from 5 minutes of continuous locomotion tracking. Scoring of path trajectories was performed blinded to genotype.

Optogenetic analysis

Behavioral assays were performed with young adults at room temperature (22°C–24°C). Animals were grown on plates seeded with OP50 containing 2.7 mM All-Trans Retinal (ATR). Animals were placed on fresh plates seeded with a thin lawn of OP50 containing ATR and allowed to acclimate for 1 minute. Dorsal-ventral position was noted prior to recording. Animals were allowed to move freely on plates and recorded with a Mitex X camera for 1 minute before stimulus, following this a Mightex LED module was used to stimulate Chrimson (625nm 14mW/cm^2) continuously for 2 minutes. Locomotion (trajectory and body bending) was recorded with WormLab (MBF Bioscience) software. A mid-point bending angle histogram was generated for each animal such that over the span of 2 minutes body angles were measured and binned by the degree of angle. Depending on starting position negative and positive degree angles were assigned dorsal or ventral. Any bending angle greater than 0 but less than 50˚ was determined a regular bend. We noted wild type animals without stimulus rarely make angles greater then 50˚ and qualified any bending angle over 50˚ as a deep bend. An ANOVA with Dunnett's multiple comparisons test was used for comparisons between pre-stimulus and stimulus in wild type and *dve-1(uf171)*. A Student's T-test was used when comparing number of dorsal bends greater then 50° in wildtype vs *dve-1* mutant animals.

RNAi by feeding

L4 larvae expressing *hsp-6pr::*GFP were cultured with *E. coli* expressing either control double-stranded RNA (empty vector) or targeting *cco-1* and progeny were allowed to develop to L4 stage at 20°C. Intestinal GFP fluorescence of L4 stage progeny was measured using the Zeiss Imager M1, 10x objective.

CRISPR/Cas9 K327R

Strain IZ4473 *dve-1(uf206)* was generated in *syb1984* (DVE-1 CRISPR-Cas9-mediated GFP knock, Tian lab) animals. A K-R mutation was created by changing AAA to CGT in exon 6, 4783 bp downstream of start. The IDT CRISPR HDR design tool (https://www.idtdna.com/pages/tools/alt-r-crispr-hdr-design-tool) was used to generate repair templates and guide sequences. Animals were injected with CRISPR/Cas9 mix [crRNA (oligo 2nmol, IDT), Donor (oligo 4nmol, IDT), purified Alt-R S.p. Cas9 nuclease V3 100µg (IDT CAT 1081058), Alt-R CRISPR/Cas9 tracrRNA (5nmol, IDT CAT 1072532), and pRF-4 (*rol-6* plasmid)]. Rolling worms were singled and validated by PCR sequencing. CRISPR/Cas9 design is provided in supplemental file 4.

DVE-1 nuclear localization

DVE-1::GFP was measured in L1 stage DD nuclei using the strain *syb1984* (DVE-1 CRISPR-Cas9-mediated GFP knock in); *ufEx1814*(*unc-47pr::NLS::mCherry*). ROIs were determined by expression of the nuclear localized mCherry signal. Within the ROI a segmented line was drawn through the nucleus and an intensity profile was created for each nucleus. Fluorescence intensity values for DVE-1::GFP were quantified by averaging the largest 5 intensity values at the peak (roughly 0.5 µm). At least 2 DD nuclei per animal were analyzed. ANOVA with Dunnett's multiple

comparison test was used for statistical analysis. For analysis of *unc-30* mutants, an ROI was selected from the base of the pharynx out posteriorly by 30µm. For consistent analysis red GABA neurons within the head, unaffected by *unc-30* mutation and the pharynx served as landmarks for both wild type and *unc-30* mutant animals. Students t-test was used for statistical analysis.

ChIP-seq data acquisition from ModEncode

modENCODE (www.modencode.org) produced ChIP-seq data by immunoprecipitating GFP from a line expressing DVE-1::GFP that was stably integrated into the genome. The DVE-1 ChIP-seq data set included two biological replicates at the late embryo stage as well as control animals. Significant peaks were called using PeakSeq and only peaks that were identified in both biological replicates were considered for analysis. DVE-1::GFP ChIP-seq data and experimental details can be found at http://intermine.modencode.org/release-33/report.do?id=77000654 (DCCid: modENCODE_4804) [85, 86]. Peaks were considered mapped to genes if there was at least an 80% overlap between the peak maximum read density and the region within 1kb base pairs upstream of the genes annotated transcriptional start site using the UCSC table browser intersect function [87].

Pathway analysis

Pathway analysis was performed using both WormCat [56]: http://www.wormcat.com, and the enrichment analysis tool WormenrichR [57, 58]: https://amp.pharm.mssm.edu/WormEnrichr/. For WormCat analysis pathways were considered enriched if they had a p-value < 0.01 and Bonferroni FDR < 0.01. The WormEnrichR pathway enrichment analysis utilized both the Kyoto Encyclopedia of Genes and Genomes (KEGG) database [88] and the WikiPathway database

[89]. For WormEnrichR, pathways were considered enriched if they had a p-adj < 0.05 and a combined score >10.

Drosophila Mushroom Body Expression

Dve expression analysis in *Drosophila* mushroom body gamma neurons was described previously [66] (https://www.weizmann.ac.il/mcb/Schuldiner/resources) .

References

1. Crepel, F., J. Mariani, and N. Delhaye-Bouchaud, Evidence for a multiple innervation of Purkinje cells by climbing fibers in the immature rat cerebellum. Journal of neurobiology, 1976. **7**(6): p. 567-578.
2. Hong, Y.K., et al., Refinement of the retinogeniculate synapse by bouton clustering. Neuron, 2014. **84**(2): p. 332-339.
3. Hubel, D.H., et al., Plasticity of ocular dominance columns in monkey striate cortex. Philosophical Transactions of the Royal Society of London. B, Biological Sciences, 1977. **278**(961): p. 377-409.
4. Technau, G. and M. Heisenberg, Neural reorganization during metamorphosis of the corpora pedunculata in Drosophila melanogaster. Nature, 1982. **295**(5848): p. 405-407.
5. Walsh, M.K. and J.W. Lichtman, In vivo time-lapse imaging of synaptic takeover associated with naturally occurring synapse elimination. Neuron, 2003. **37**(1): p. 67-73.
6. Paolicelli, R.C., et al., Synaptic pruning by microglia is necessary for normal brain development. science, 2011. **333**(6048): p. 1456-1458.
7. Schafer, D., et al., Microglia sculpt postnatal neural circuits in an activity and complement-dependent manner. Neuron, 2012. **74**(4): p. 691-705.
8. Tremblay, M.-È., R.L. Lowery, and A.K. Majewska, Microglial interactions with synapses are modulated by visual experience. PLoS biology, 2010. **8**(11): p. e1000527.

9. Wake, H., et al., Resting microglia directly monitor the functional state of synapses in vivo and determine the fate of ischemic terminals. Journal of Neuroscience, 2009. **29**(13): p. 3974-3980.

10. Kobayashi, Y., Z. Ye, and T.K. Hensch, Clock genes control cortical critical period timing. Neuron, 2015. **86**(1): p. 264-275.

11. Feinberg, I., Schizophrenia: caused by a fault in programmed synaptic elimination during adolescence? Journal of psychiatric research, 1982. **17**(4): p. 319-334.

12. Hong, S., et al., Complement and microglia mediate early synapse loss in Alzheimer mouse models. Science, 2016. **352**(6286): p. 712-716.

13. Knobloch, M. and I.M. Mansuy, Dendritic spine loss and synaptic alterations in Alzheimer's disease. Molecular neurobiology, 2008. **37**(1): p. 73-82.

14. Sekar, A., et al., Schizophrenia risk from complex variation of complement component 4. Nature, 2016. **530**(7589): p. 177-183.

15. Sun, D., et al., Brain surface contraction mapped in first-episode schizophrenia: a longitudinal magnetic resonance imaging study. Molecular psychiatry, 2009. **14**(10): p. 976-986.

16. Yaron, A. and O. Schuldiner, Common and divergent mechanisms in developmental neuronal remodeling and dying back neurodegeneration. Current Biology, 2016. **26**(13): p. R628-R639.

17. Sulston, J.E., Post-embryonic development in the ventral cord of Caenorhabditis elegans. Philosophical Transactions of the Royal Society of London. B, Biological Sciences, 1976. **275**(938): p. 287-297.

18. White, J.G., et al., The structure of the nervous system of the nematode Caenorhabditis elegans. Philos Trans R Soc Lond B Biol Sci, 1986. **314**(1165): p. 1-340.

19. Cuentas-Condori, A. and r. Miller, David M, Synaptic remodeling, lessons from C. elegans. Journal of neurogenetics, 2020. **34**(3-4): p. 307-322.

20. Kurup, N. and Y. Jin. Neural circuit rewiring: insights from DD synapse remodeling. in Worm. 2016. Taylor & Francis.

21. White, J.G., D. Albertson, and M. Anness, Connectivity changes in a class of motoneurone during the development of a nematode. Nature, 1978. **271**(5647): p. 764-766.

22. Hallam, S.J. and Y. Jin, lin-14 regulates the timing of synaptic remodelling in Caenorhabditis elegans. Nature, 1998. **395**(6697): p. 78-82.

23. Meng, J., et al., Myrf ER-bound transcription factors drive C. elegans synaptic plasticity via cleavage-dependent nuclear translocation. Developmental cell, 2017. **41**(2): p. 180-194. e7.

24. Miller-Fleming, T.W., et al., Transcriptional control of parallel-acting pathways that remove specific presynaptic proteins in remodeling neurons. Journal of Neuroscience, 2021. **41**(27): p. 5849-5866.

25. Miller-Fleming, T.W., et al., The DEG/ENaC cation channel protein UNC-8 drives activity-dependent synapse removal in remodeling GABAergic neurons. Elife, 2016. **5**: p. e14599.

26. Thompson-Peer, K.L., et al., HBL-1 patterns synaptic remodeling in C. elegans. Neuron, 2012. **73**(3): p. 453-465.

27. Park, M., et al., CYY-1/cyclin Y and CDK-5 differentially regulate synapse elimination and formation for rewiring neural circuits. Neuron, 2011. **70**(4): p. 742-757.

28. He, S., et al., Transcriptional control of synaptic remodeling through regulated expression of an immunoglobulin superfamily protein. Current Biology, 2015. **25**(19): p. 2541-2548.

29. Howell, K., J.G. White, and O. Hobert, Spatiotemporal control of a novel synaptic organizer molecule. Nature, 2015. **523**(7558): p. 83-87.

30. Petrash, H.A., et al., ACR-12 ionotropic acetylcholine receptor complexes regulate inhibitory motor neuron activity in Caenorhabditis elegans. Journal of Neuroscience, 2013. **33**(13): p. 5524-5532.

31. Haynes, C.M., et al., ClpP mediates activation of a mitochondrial unfolded protein response in C. elegans. Developmental cell, 2007. **13**(4): p. 467-480.

32. Jumper, J., et al., Highly accurate protein structure prediction with AlphaFold. Nature, 2021. **596**(7873): p. 583-589.

33. Varadi, M., et al., AlphaFold Protein Structure Database: massively expanding the structural coverage of protein-sequence space with high-accuracy models. Nucleic acids research, 2022. **50**(D1): p. D439-D444.

34. Gally, C., et al., A transmembrane protein required for acetylcholine receptor clustering in Caenorhabditis elegans. Nature, 2004. **431**(7008): p. 578-582.

35. He, S., A. Cuentas-Condori, and D.M. Miller III, NATF (Native and Tissue-Specific Fluorescence): a strategy for bright, tissue-specific GFP labeling of native proteins in Caenorhabditis elegans. Genetics, 2019. **212**(2): p. 387-395.

36. Cuentas-Condori, A., et al., C. elegans neurons have functional dendritic spines. Elife, 2019. **8**: p. e47918.

37. Oliver, D., et al., Kinesin-3 mediated axonal delivery of presynaptic neurexin stabilizes dendritic spines and postsynaptic components. PLoS genetics, 2022. **18**(1): p. e1010016.

38. Philbrook, A., et al., Neurexin directs partner-specific synaptic connectivity in C. elegans. elife, 2018. **7**: p. e35692.

39. Gottschalk, A. and W.R. Schafer, Visualization of integral and peripheral cell surface proteins in live Caenorhabditis elegans. Journal of neuroscience methods, 2006. **154**(1-2): p. 68-79.

40. Klapoetke, N.C., et al., Independent optical excitation of distinct neural populations. Nature methods, 2014. **11**(3): p. 338-346.

41. Larsch, J., et al., A circuit for gradient climbing in C. elegans chemotaxis. Cell reports, 2015. **12**(11): p. 1748-1760.

42. Chen, T.-W., et al., Ultrasensitive fluorescent proteins for imaging neuronal activity. Nature, 2013. **499**(7458): p. 295-300.

43. Varshney, L.R., et al., Structural properties of the Caenorhabditis elegans neuronal network. PLoS computational biology, 2011. **7**(2): p. e1001066.

44. Nguyen, M., et al., Caenorhabditis elegans mutants resistant to inhibitors of acetylcholinesterase. Genetics, 1995. **140**(2): p. 527-535.

45. Zhu, D., et al., NuRD mediates mitochondrial stress–induced longevity via chromatin remodeling in response to acetyl-CoA level. Science advances, 2020. **6**(31): p. eabb2529.

46. Reilly, M.B., et al., Unique homeobox codes delineate all the neuron classes of C. elegans. Nature, 2020. **584**(7822): p. 595-601.

47. Cinar, H., S. Keles, and Y. Jin, Expression profiling of GABAergic motor neurons in Caenorhabditis elegans. Current Biology, 2005. **15**(4): p. 340-346.

48. Shan, G., et al., Convergent genetic programs regulate similarities and differences between related motor neuron classes in Caenorhabditis elegans. Developmental biology, 2005. **280**(2): p. 494-503.

49. Yu, B., et al., Convergent transcriptional programs regulate cAMP levels in C. elegans GABAergic motor neurons. Developmental Cell, 2017. **43**(2): p. 212-226. e7.

50. Gao, K., et al., SUMO peptidase ULP-4 regulates mitochondrial UPR-mediated innate immunity and lifespan extension. Elife, 2019. **8**: p. e41792.

51. Dobreva, G., J. Dambacher, and R. Grosschedl, SUMO modification of a novel MAR-binding protein, SATB2, modulates immunoglobulin μ gene expression. Genes & development, 2003. **17**(24): p. 3048-3061.

52. Tan, J.-A.T., et al., Phosphorylation-dependent interaction of SATB1 and PIAS1 directs SUMO-regulated caspase cleavage of SATB1. Molecular and cellular biology, 2010. **30**(11): p. 2823-2836.

53. Boyle, A.P., et al., Comparative analysis of regulatory information and circuits across distant species. Nature, 2014. **512**(7515): p. 453-456.

54. Hammarlund, M., et al., The CeNGEN project: the complete gene expression map of an entire nervous system. Neuron, 2018. **99**(3): p. 430-433.

55. Taylor, S.R., et al., Molecular topography of an entire nervous system. Cell, 2021. **184**(16): p. 4329-4347. e23.

56. Holdorf, A.D., et al., WormCat: an online tool for annotation and visualization of Caenorhabditis elegans genome-scale data. Genetics, 2020. **214**(2): p. 279-294.

57. Chen, E.Y., et al., Enrichr: interactive and collaborative HTML5 gene list enrichment analysis tool. BMC bioinformatics, 2013. **14**(1): p. 1-14.

58. Kuleshov, M.V., et al., Enrichr: a comprehensive gene set enrichment analysis web server 2016 update. Nucleic acids research, 2016. **44**(W1): p. W90-W97.

59. Tian, Y., et al., Mitochondrial stress induces chromatin reorganization to promote longevity and UPRmt. Cell, 2016. **165**(5): p. 1197-1208.

60. Wu, Z., et al., Mitochondrial unfolded protein response transcription factor ATFS-1 promotes longevity in a long-lived mitochondrial mutant through activation of stress response pathways. BMC biology, 2018. **16**(1): p. 1-19.

61. Yang, W. and S. Hekimi, A mitochondrial superoxide signal triggers increased longevity in Caenorhabditis elegans. PLoS biology, 2010. **8**(12): p. e1000556.

62. Benedetti, C., et al., Ubiquitin-like protein 5 positively regulates chaperone gene expression in the mitochondrial unfolded protein response. Genetics, 2006. **174**(1): p. 229-239.

63. Chang, C.-W., et al., Distinct stages of synapse elimination are induced by burst firing of CA1 neurons and differentially require MEF2A/D. Elife, 2017. **6**: p. e26278.

64. Flavell, S.W., et al., Activity-dependent regulation of MEF2 transcription factors suppresses excitatory synapse number. Science, 2006. **311**(5763): p. 1008-1012.

65. Flavell, S.W., et al., Genome-wide analysis of MEF2 transcriptional program reveals synaptic target genes and neuronal activity-dependent polyadenylation site selection. Neuron, 2008. **60**(6): p. 1022-1038.

66. Alyagor, I., et al., Combining developmental and perturbation-seq uncovers transcriptional modules orchestrating neuronal remodeling. Developmental cell, 2018. **47**(1): p. 38-52. e6.

67. Balamotis, M.A., et al., Satb1 ablation alters temporal expression of immediate early genes and reduces dendritic spine density during postnatal brain development. Molecular and cellular biology, 2012. **32**(2): p. 333-347.

68. Alcamo, E.A., et al., Satb2 regulates callosal projection neuron identity in the developing cerebral cortex. Neuron, 2008. **57**(3): p. 364-377.

69. Turovsky, E.A., et al., Role of Satb1 and Satb2 transcription factors in the glutamate receptors expression and Ca2+ signaling in the cortical neurons in vitro. International journal of molecular sciences, 2021. **22**(11): p. 5968.

70. Den Hoed, J., et al., Mutation-specific pathophysiological mechanisms define different neurodevelopmental disorders associated with SATB1 dysfunction. The American Journal of Human Genetics, 2021. **108**(2): p. 346-356.

71. Zarate, Y.A., et al., Mutation update for the SATB2 gene. Human mutation, 2019. **40**(8): p. 1013-1029.

72. Zarate, Y.A., et al., Natural history and genotype-phenotype correlations in 72 individuals with SATB2-associated syndrome. American Journal of Medical Genetics Part A, 2018. **176**(4): p. 925-935.

73. di Sanguinetto, S.A.D.T., J.S. Dasen, and S. Arber, Transcriptional mechanisms controlling motor neuron diversity and connectivity. Current opinion in neurobiology, 2008. **18**(1): p. 36-43.

74. Rister, J., C. Desplan, and D. Vasiliauskas, Establishing and maintaining gene expression patterns: insights from sensory receptor patterning. Development, 2013. **140**(3): p. 493-503.

75. Srinivasan, K., et al., A network of genetic repression and derepression specifies projection fates in the developing neocortex. Proceedings of the National Academy of Sciences, 2012. **109**(47): p. 19071-19078.

76. Swaroop, A., D. Kim, and D. Forrest, Transcriptional regulation of photoreceptor development and homeostasis in the mammalian retina. Nature Reviews Neuroscience, 2010. **11**(8): p. 563-576.

77. Viets, K., K.C. Eldred, and R.J. Johnston Jr, Mechanisms of photoreceptor patterning in vertebrates and invertebrates. Trends in Genetics, 2016. **32**(10): p. 638-659.

78. Mello, C.C., et al., Efficient gene transfer in C. elegans: extrachromosomal maintenance and integration of transforming sequences. The EMBO journal, 1991. **10**(12): p. 3959-3970.

79. Jorgensen, E.M. and S.E. Mango, The art and design of genetic screens: Caenorhabditis elegans. Nature Reviews Genetics, 2002. **3**(5): p. 356-369.

80. Minevich, G., et al., CloudMap: a cloud-based pipeline for analysis of mutant genome sequences. Genetics, 2012. **192**(4): p. 1249-1269.

81. Doitsidou, M., S. Jarriault, and R.J. Poole, Next-generation sequencing-based approaches for mutation mapping and identification in Caenorhabditis elegans. Genetics, 2016. **204**(2): p. 451-474.

82. Burnett, K., E. Edsinger, and D.R. Albrecht, Rapid and gentle hydrogel encapsulation of living organisms enables long-term microscopy over multiple hours. Communications biology, 2018. **1**(1): p. 1-10.

83. Yemini, E., R.A. Kerr, and W.R. Schafer, Preparation of samples for single-worm tracking. Cold Spring Harbor Protocols, 2011. **2011**(12): p. pdb. prot066993.

84. Yemini, E., et al., A database of Caenorhabditis elegans behavioral phenotypes. Nature methods, 2013. **10**(9): p. 877-879.

85. Gerstein, M.B., et al., Integrative analysis of the Caenorhabditis elegans genome by the modENCODE project. Science, 2010. **330**(6012): p. 1775-1787.

86. Sarov, M., et al., A genome-scale resource for in vivo tag-based protein function exploration in C. elegans. Cell, 2012. **150**(4): p. 855-866.

87. Karolchik, D., et al., The UCSC Table Browser data retrieval tool. Nucleic acids research, 2004. **32**(suppl_1): p. D493-D496.

88. Kanehisa, M. and S. Goto, KEGG: kyoto encyclopedia of genes and genomes. Nucleic acids research, 2000. **28**(1): p. 27-30.

89. Martens, M., et al., WikiPathways: connecting communities. Nucleic acids research, 2021. **49**(D1): p. D613-D621.

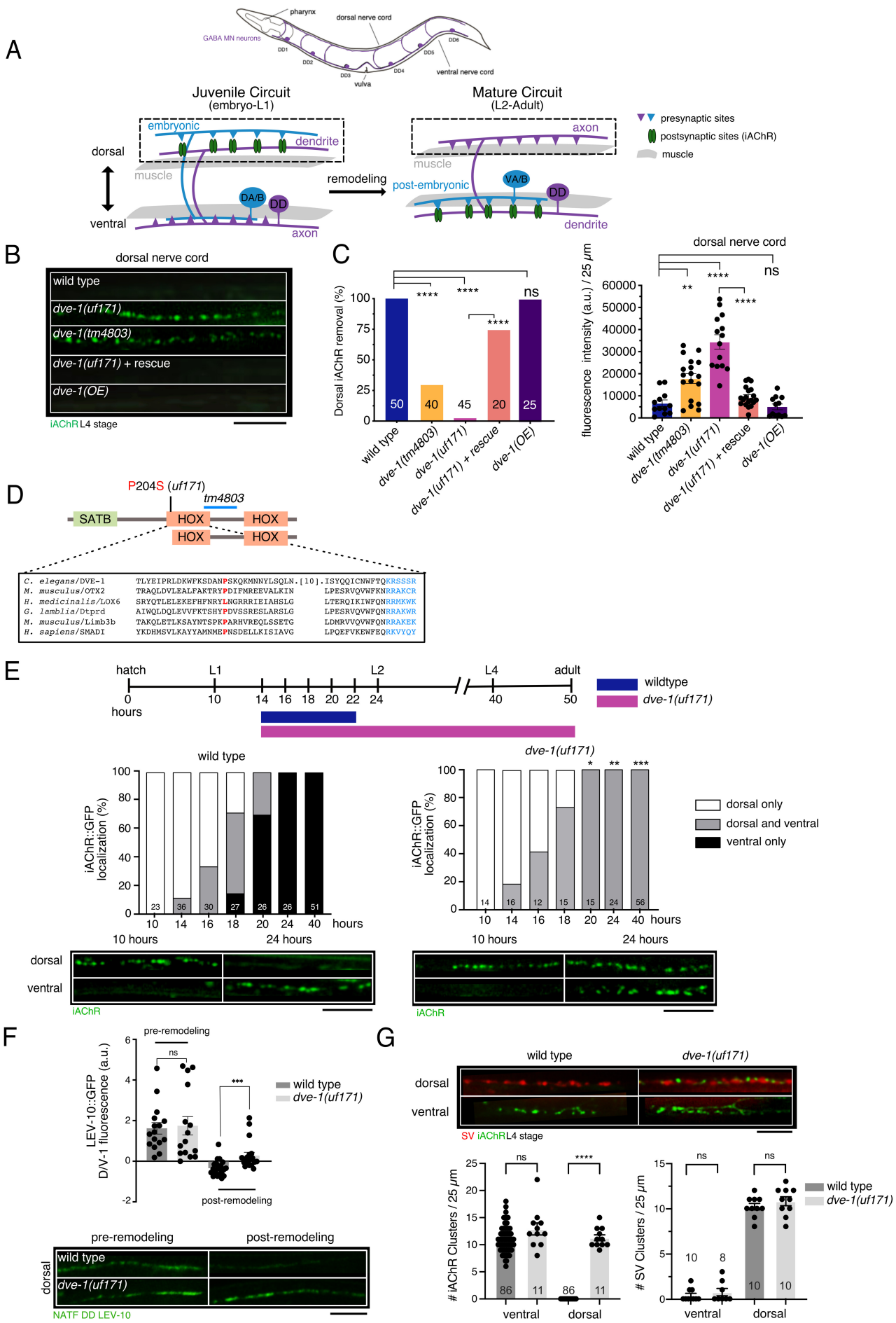
A
pharynx
dorsal nerve cord
GABA MN neurons
DD1
DD2
DD3
DD4
DD5
DD6
vulva
ventral nerve cord
Juvenile Circuit
(embryo-L1)
Mature Circuit
(L2-Adult)
presynaptic sites
postsynaptic sites (iAChR)
muscle
embryonic
dendrite
dorsal
ventral
muscle
DA/B
DD
axon
remodeling
post-embryonic
VA/B
DD
dendrite
B
dorsal nerve cord
wild type
dve-1(uf171)
dve-1(tm4803)
dve-1(uf171) + rescue
dve-1(OE)
iAChR L4 stage
C
Dorsal iAChR removal (%)
100
75
50
25
0
****
****
****
ns
50
40
45
20
25
wild type
dve-1(tm4803)
dve-1(uf171)
dve-1(uf171) + rescue
dve-1(OE)
dorsal nerve cord
fluorescence intensity (a.u.) / 25 µm
60000
50000
40000
30000
20000
10000
0
**
****
****
ns
wild type
dve-1(tm4803)
dve-1(uf171)
dve-1(uf171) + rescue
dve-1(OE)
D
P204S (uf171)
tm4803
SATB
HOX
HOX
HOX
HOX
C. elegans/DVE-1 TLYEIPRLDKWFKSDANPSKQKMNNYLSQLN.[10].ISYQQICNWFTQKRSSSR
M. musculus/OTX2 TRAQLDVLEALFAKTRYPDIFMREEVALKIN LPESRVQVWFKNRRAKCR
H. medicinalis/LOX6 SRYQTLELEKEFHFNRYLNGRRRIEIAHSLG LTERQIKIWFQNRRMKWK
G. lamblia/Dtprd AIWQLDQLEVVFKTSHYPDVSSRESLARSLG LPESRVQVWFQNRRAKWR
M. musculus/Limb3b TAKQLETLKSAYNTSPKPARHVREQLSSETG LDMRVVQVWFQNRRAKEK
H. sapiens/SMADI YKDHMSVLKAYYAMNMEPNSDELLKISIAVG LPQEFVKEWFEQRKVYQY
E
hatch
L1
L2
L4
adult
0
10
14
16
18
20
22
24
40
50
hours
wildtype
dve-1(uf171)
wild type
iAChR::GFP localization (%)
100
80
60
40
20
0
23
36
30
27
26
26
51
10
14
16
18
20
24
40
hours
10 hours
24 hours
dve-1(uf171)
*
**
***
14
16
12
15
15
24
56
dorsal only
dorsal and ventral
ventral only
dorsal
ventral
iAChR
iAChR
F
pre-remodeling
LEV-10::GFP D/V-1 fluorescence (a.u.)
6
4
2
0
-2
ns
***
post-remodeling
wild type
dve-1(uf171)
pre-remodeling
post-remodeling
dorsal
wild type
dve-1(uf171)
NATF DD LEV-10
G
wild type
dve-1(uf171)
dorsal
ventral
SV iAChR L4 stage
iAChR Clusters / 25 µm
25
20
15
10
5
0
ns
****
86
11
86
11
ventral
dorsal
SV Clusters / 25 µm
15
10
5
0
ns
ns
10
8
10
10
ventral
dorsal
wild type
dve-1(uf171)

Figure 1. Mutations in the homeodomain transcription factor DVE-1 disrupt the removal of postsynaptic sites in GABAergic motor neurons

(A) Top, schematic of *C. elegans* labeling DD GABAergic motor neurons (purple). Bottom, schematic depicting motor circuit remodeling. Left, embryonic DD motor neurons (purple) receive input from cholinergic motor neurons (blue) in the dorsal nerve cord and make synaptic contacts onto ventral muscles. Right, after the L1-L2 molt, DD motor neurons are remodeled to receive inputs from postembryonic born cholinergic motor neurons in the ventral nerve cord and make synaptic contacts onto dorsal muscles..

(B) Fluorescent confocal images of synaptic ACR-12::GFP clusters (iAChRs, green) in GABAergic DD processes of the dorsal nerve cord at L4 stage. By L4 stage, iAChR clusters are completely eliminated from the dorsal nerve cord of wild type animals. In contrast, iAChR clusters remain present in the dorsal nerve cord of *dve-1* mutants. Rescue refers to expression of genomic sequence encoding wild type DVE-1. OE refers to overexpression of *dve-1* in the wild type. In this and subsequent figures, iAChR refers to ACR-12::GFP unless otherwise indicated. Scale bar, 5 μm.

(C) Quantification of iAChR clustering at L4 stage for the genotypes indicated. Left, bars represent the percentage of L4 stage animals where dorsal iAChRs have been completely removed. ****p<0.0001, Fischer's exact test with Bonferroni Correction. For this and subsequent figures, numbers within bars indicate the number of animals scored for each condition. Right, measures of average fluorescence intensity per 25 μm in the dorsal nerve cord. Bars indicate mean ± SEM. **p<0.05, ****p<0.0001, ns – not significant ANOVA with Dunnett's multiple comparisons test. Each point represents a single animal. The number of animals >10 per genotype.

(D) Domain structure of DVE-1. SATB-like domain and homeodomains (HOX) are indicated. Site of substitution produced by *uf171* missense mutation (red) and region of *tm4803*

deletion mutation (blue) are indicated. Inset, sequence alignment of homeodomain 1 (determined using NCBI Blast Conserved Domains).

(E) Top, timeline of remodeling, approximate timing of transitions between larval stages and adulthood are indicated. Bars indicate duration of DD synaptic remodeling for wild type (blue) and *dve-1* mutants (magenta). Elimination of dorsal cord iAChR clusters is completed by 22 hours after hatch for wild type whereas dorsal iAChR clusters persist through adulthood in *dve-1* mutants. Middle, quantification of iAChR remodeling in DD neurons of wild type (left) and *dve-1* mutants (right). X-axis time from hatching in hours. Animals are binned according to the distribution of iAChR puncta as dorsal only (white), ventral only (black), or dorsal and ventral (grey). Bottom, representative images of dorsal and ventral iAChR clusters for wild type (left) and *dve-1* mutants (right) at the times indicated. *$p<0.05$, ** $p<0.01$, *** $p<0.001$, Fischer's exact test. Scale bar, 5 μm.

(F) Top, scatterplot of LEV-10::GFP dorsal/ventral fluorescence intensity ratio measurements per corresponding 25 μm regions of dorsal and ventral nerve cord expressed as dorsal/ventral fluorescence ratio -1. Values greater than zero indicate predominant dorsal localization while values less than zero indicate predominant ventral localization. The postsynaptic scaffold LEV-10::GFP is incompletely removed from dorsal nerve cord in *dve-1(uf171)* mutants. Bars indicate mean ± SEM. ***$p<0.001$, ns – not significant student's t-test. Bottom, confocal images of LEV-10::GFP from the dorsal nerve cord before (pre-remodeling) and after (post-remodeling) the L1/L2 transition. Scale bar, 5 μm. NATF DD LEV-10 indicates tissue-specific labeling of endogenous LEV-10 [35]. Each point represents a single animal. The number of animals >10 per genotype.

(G) Top, confocal images of the dorsal and ventral process from L4 stage wild type and *dve-1(uf171)* mutants co-expressing the synaptic vesicle marker mCherry::RAB-3 (SV) and ACR-12::GFP marker (iAChR) in DD neurons. Scale bar, 5 μm. Bottom, quantification of iAChR clusters (left) and SV puncta (right) in dorsal and ventral processes of L4 stage DD

neurons for wild type and *dve-1(uf171)* mutants. iAChRs in DD neurons are not eliminated from the dorsal nerve cord of L4 stage *dve-1* mutants, but new clusters form normally in the ventral nerve cord. SV clusters are properly reoriented from the ventral cord to the dorsal nerve cord in DD neurons of *dve-1* mutants. Bars indicate mean ± SEM. Student's t-test, ****$p<0.0001$, ns – not significant. Each point represents a single animal.

Table 1: Mutations that delay GABAergic presynaptic remodeling do not affect cholinergic postsynaptic remodeling in DD motor neurons

AChR (*flp-13pr*::ACR-12::GFP)

genotype (L4 stage)	percent remodeled (ventral only) (n)	percent not remodeled (dorsal only + both sides)	total (n)	Fischer's Exact P-Value	Bonferroni correction (significant?) α <0.003
wild type	100 (93)	0 (0)	93		
ced-3(ok2734)[23]	100 (21)	0 (0)	21	1	no
ced-3(n717) [23]	100 (23)	0 (0)	23	1	no
cdk-5(ok626)[27]	100 (20)	0 (0)	20	1	no
unc-8(e49) [25]	100 (20)	0 (0)	20	1	no
unc-8(e15) [25]	100 (10)	0 (0)	10	1	no

SV *(flp-13pr*::mCherry::RAB-3)

genotype (L4 stage)	percent remodeled (dorsal only) (n)	percent not remodeled (ventral only + both sides)	total (n)	Fischer's Exact P-Value	Bonferroni correction (significant?) α <0.01
wild type	100 (30)	0 (0)	30		
ced-3(ok2734)[23]	56 (6)	44 (5)	11	0.0006	yes
ced-3(n717) [23]	57 (13)	43 (10)	23	0.0001	yes
cdk-5(ok626)[27]	36 (4)	64 (7)	11	0.0001	yes
unc-8(e49) [25]	56 (9)	44 (7)	16	0.0002	yes
unc-8(e15) [25]	60 (6)	40 (4)	10	0.0023	yes

Table 2: Effects of synaptic activity and calcium signaling on synaptic remodeling

AChR (*flp-13pr*::ACR-12::GFP)

genotype (24hrs post-hatch)	percent remodeled (ventral only) (n)	percent not remodeled (dorsal only + both sides)	total (n)	Fischer's Exact P-Value	Bonferroni correction (significant?) α <0.0055
wild type	96 (64)	4 (3)	67		
unc-2(e55)[25]	100 (10)	0 (0)	10	1	no
cca-1(ad1650)	100 (17)	0 (0)	17	1	no
itr-1(sa73)	100 (18)	0 (0)	18	1	no
unc-68(e540)	50 (6)	50 (6)	12	0.0002	yes
unc-13(e51)	100 (11)	0 (0)	11	1	no
unc-43(e408)	95 (19)	5 (1)	20	1	no
unc-18(e234)[26]	100 (10)	0 (0)	10	1	no
unc-17(e113)	76 (13)	24 (4)	17	0.0284	no

genotype (L4 stage)	percent remodeled (ventral only) (n)	percent not remodeled (dorsal only + both sides)	total (n)	Fischer's Exact P-Value	Bonferroni correction (significant?) α <0.003
wild type	100 (93)	0 (0)	93		
unc-2(e55)[25]	100 (10)	0 (0)	10	1	no
unc-2(zf35)[25]	86 (6)	14 (1)	7	0.07	no
cca-1(ad1650)	100 (10)	0 (0)	10	1	no
itr-1(sa73)	100 (10)	0 (0)	10	1	no
unc-68(e540)	100 (11)	0 (0)	11	1	no
unc-43(e408)	100 (9)	0 (0)	9	1	no
unc-43 (n498)	100 (14)	0 (0)	14	1	no
unc-18(e234)[26]	100 (8)	0 (0)	8	1	no
unc-31 (e928)[26]	100 (10)	0 (0)	10	1	no
unc-17(e113)	100 (11)	0 (0)	11	1	no

SV (*flp-13pr*::mCherry::RAB-3)

genotype (24hrs post-hatch)	Percent remodeled (dorsal only) (n)	percent not remodeled (ventral only + both sides)	total (n)	Fischer's Exact P-Value	Bonferroni correction (significant?) α <0.025
wild type	97 (28)	3 (1)	29		
unc-18(e234)[26]	40 (4)	60 (6)	10	0.0004	yes
unc-17(e113)	33 (2)	67 (4)	6	0.0014	yes

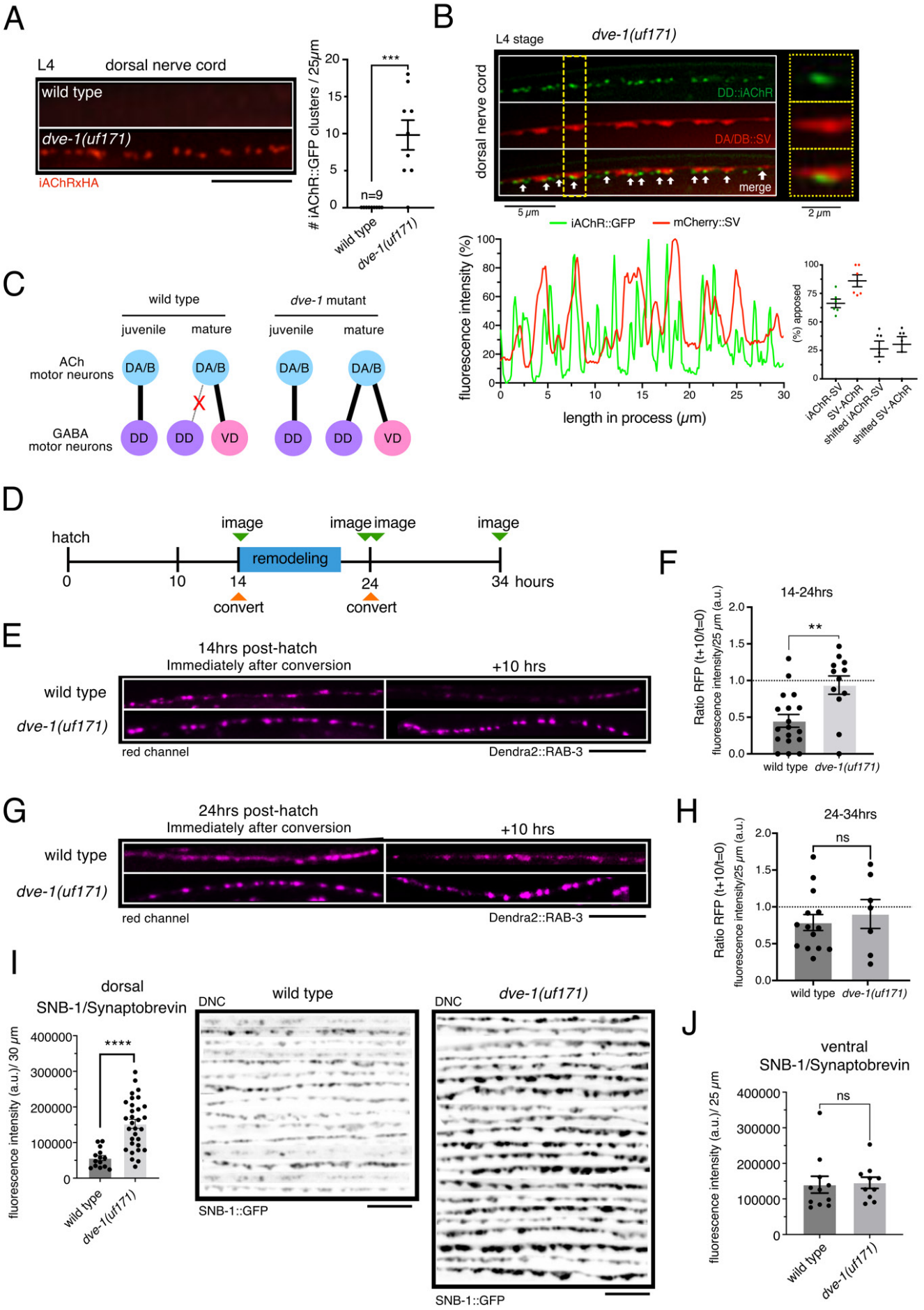
A
L4
dorsal nerve cord
wild type
dve-1(uf171)
iAChRxHA
iAChR::GFP clusters / 25μm
***
n=9
wild type
dve-1(uf171)
B
L4 stage
dve-1(uf171)
dorsal nerve cord
DD::iAChR
DA/DB::SV
merge
5 μm
2 μm
iAChR::GFP
mCherry::SV
fluorescence intensity (%)
length in process (μm)
(%) apposed
iAChR-SV
SV-AChR
shifted iAChR-SV
shifted SV-AChR
C
wild type
dve-1 mutant
juvenile
mature
ACh motor neurons
GABA motor neurons
DA/B
DD
VD
D
hatch
image
image image
image
remodeling
0
10
14
24
34 hours
convert
convert
E
14hrs post-hatch
Immediately after conversion
+10 hrs
wild type
dve-1(uf171)
red channel
Dendra2::RAB-3
F
14-24hrs
**
Ratio RFP (t+10/t=0)
fluorescence intensity/25 μm (a.u.)
wild type
dve-1(uf171)
G
24hrs post-hatch
Immediately after conversion
+10 hrs
wild type
dve-1(uf171)
red channel
Dendra2::RAB-3
H
24-34hrs
ns
Ratio RFP (t+10/t=0)
fluorescence intensity/25 μm (a.u.)
wild type
dve-1(uf171)
I
dorsal
SNB-1/Synaptobrevin
****
fluorescence intensity (a.u.)/ 30 μm
wild type
dve-1(uf171)
DNC
wild type
SNB-1::GFP
DNC
dve-1(uf171)
SNB-1::GFP
J
ventral
SNB-1/Synaptobrevin
ns
fluorescence intensity (a.u.)/ 25 μm
wild type
dve-1(uf171)

Figure 2: Mutation of *dve-1* enhances stability of cholinergic presynaptic sites

(A) Left, fluorescent confocal images of L4 stage cell surface iAChR clusters in the dorsal nerve cord labeled by anti-HA antibody fluorescence (red). Scale bar, 5 µm. Right, scatterplot of average number of dorsal receptor clusters per 25 µm. Each point represents a single animal n=9 for both genotypes. Data points represent mean ± SEM. ***p<0.001, students t-test.

(B) Top, merged fluorescent confocal images of L4 stage *dve-1* mutant dorsal nerve cord showing lingering clusters of juvenile postsynaptic iAChRs (*flp-13pr*::ACR-12::GFP, green) in the DD neurons and synaptic vesicles (SV, *unc-129pr*::mCherry::RAB-3, red) in presynaptic cholinergic DA/DB neurons. Dashed yellow line indicates area shown in inset (right). Bottom, line scan (left) and quantification (right) indicating % apposition of postsynaptic iAChR and presynaptic cholinergic vesicle clusters. Line scan indicates relative fluorescence intensity of iAChR (green) and SV (red) for a 30 µm region of L4 stage *dve-1* mutant dorsal nerve cord. Scatterplot shows the percentage apposition between iAChR clusters in DD motor neurons and cholinergic synaptic vesicle puncta in DA/B motor neurons (green). As controls (black) each iAChR and SV line scan was shifted by 2 µm and reassessed to determine percent apposed by chance. Each point represents a single animal. The number of animals >5. Data points indicate mean ± SEM.

(C) Simplified schematic of DA/B synaptic output. In the juvenile circuit (L1 stage) DA/B motor neurons (blue) synapse onto DD motor neurons (purple) in both wild type (left) and *dve-1* mutants (right). In the wild type mature circuit (L2 through adulthood) DA/B connections with DD motor neurons have been removed, and new connections with postembryonic born VD motor neurons (pink) are formed (left). Grey line with red “X” indicates removal of juvenile connection. Our findings suggest that connections between cholinergic DA/B neurons and DD neurons are retained in *dve-1* mutants retain (right).

(D) Schematic of photoconversion experimental design. Animals were imaged 14 hours after hatch, prior to and immediately after photoconversion. Photoconverted animals were imaged again 10 hours later. Photoconversion was performed again 24 hours after hatch. Images were captured immediately after conversion and again 10 hours later (34 hours after hatch).

(E) Confocal images of the dorsal nerve cord of wild type (top) and *dve-1(uf171)* mutants (bottom) showing red Dendra2::RAB-3 clusters in cholinergic DA/B neurons (*unc-129pr*::Dendra2::RAB-3) either immediately after photoconversion from green to red at 14 hours after hatch (left) or 10 hours later (right). Juvenile Dendra2::RAB-3 clusters are largely removed during wild type remodeling but are more stable in *dve-1* mutants. Scale bar, 5 µm.

(F) Scatterplot showing red Dendra2::RAB-3 fluorescence intensity 10 hours after photoconversion normalized to fluorescence intensity immediately after photoconversion prior to remodeling for wild type (left) and *dve-1(uf171)* mutants (right). Each point indicates a single animal. The number of animals >10 per genotype. Bars indicate mean ± SEM. $^{**}p<0.01$, student's t-test.

(G) Confocal images of the dorsal nerve cord of wild type (top) and *dve-1(uf171)* mutants (bottom) showing red Dendra2::RAB-3 clusters in cholinergic DA/B neurons either immediately after photoconversion from green to red at 24 hours after hatch (left) or 10 hours later (right). For both wild type and *dve-1* mutants, photoconverted cholinergic Dendra2::RAB-3 clusters are more stable following remodeling compared with during remodeling. Scale bar, 5 µm.

(H) Scatterplot showing red Dendra2::RAB-3 fluorescence intensity 10 hours following photoconversion normalized to fluorescence intensity immediately after photoconversion at 24 hours after hatch (after remodeling) for wild type (left) and *dve-1(uf171)* mutants (right). Each point indicates a single animal. The number of animals >6 per genotype. Bars indicate mean ± SEM. ns - not significant, student's t-test.

(I) Left, scatterplot showing average SNB-1::GFP fluorescence intensity in L4 stage cholinergic neurons (*acr-5pr*::SNB-1::GFP) of the dorsal nerve cord (DNC) for wild type and *dve-1* mutants. Each point indicates a single animal. The number of animals >10 per genotype. Bars indicate mean ± SEM. ****$p < 0.0001$, student's t-test. Right, stacked fluorescent images of the dorsal nerve cord showing SNB-1::GFP clusters in cholinergic neurons of L4 stage wild type and *dve-1(uf171)* mutants. Images on each line are from different animals. Scale bar, 5 µm.

(J) Scatterplot of average synaptic vesicle puncta (SNB-1::GFP) per 30 µm in the ventral nerve cord of VB motor neurons of L4 stage wild type and *dve-1* mutant animals. Each point represents a single animal. At least 10 animals per genotype. Bars indicate mean ± SEM. ns - not significant, student's t-test.

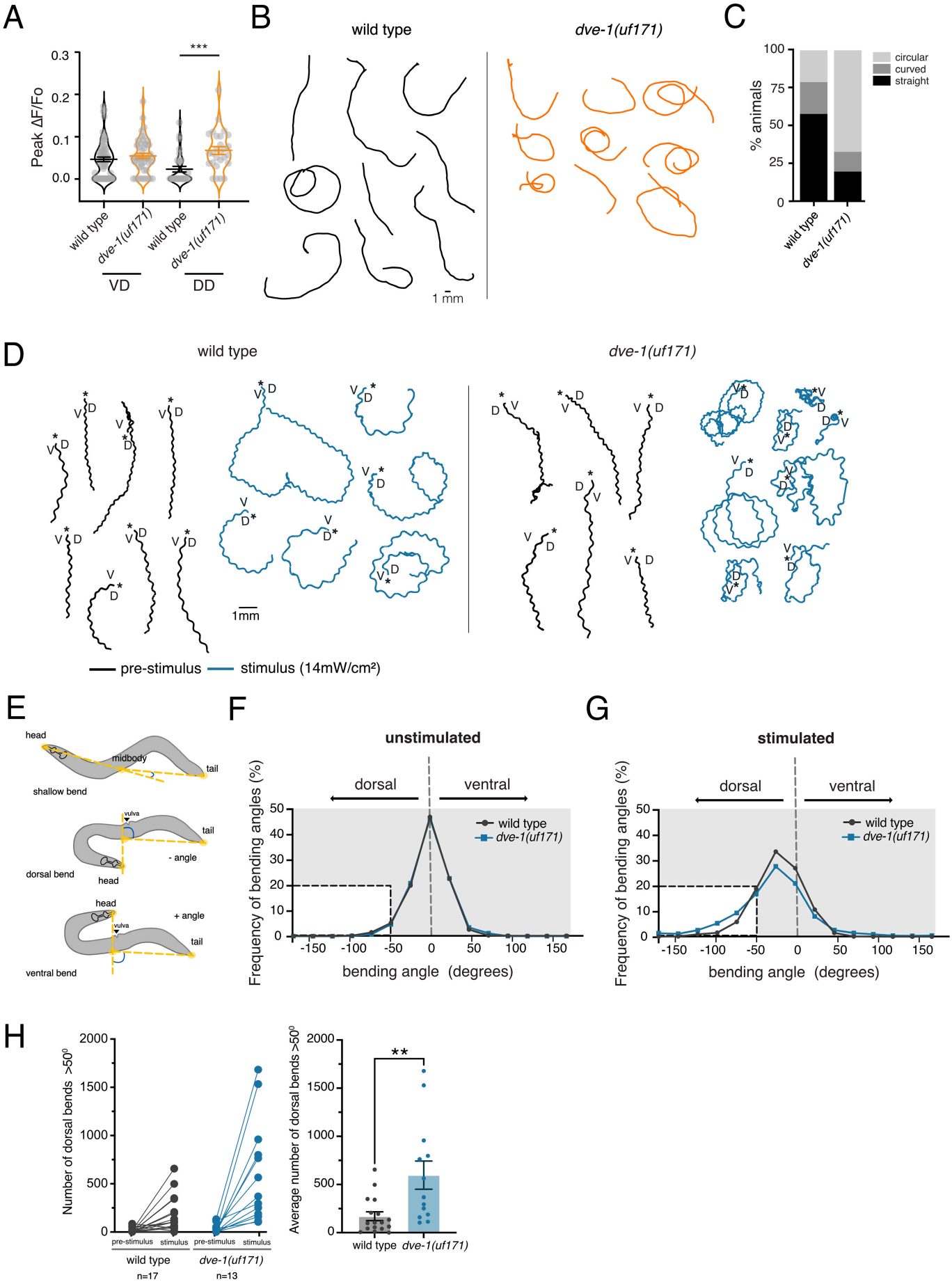
A
Peak ΔF/Fo
0.3
0.2
0.1
0.0
***
wild type
dve-1(uf171)
wild type
dve-1(uf171)
VD
DD
B
wild type
dve-1(uf171)
1 mm
C
% animals
100
75
50
25
0
circular
curved
straight
wild type
dve-1(uf171)
D
wild type
dve-1(uf171)
1mm
pre-stimulus
stimulus (14mW/cm²)
E
head
midbody
tail
shallow bend
vulva
tail
- angle
dorsal bend
head
head
+ angle
vulva
tail
ventral bend
F
unstimulated
dorsal
ventral
wild type
dve-1(uf171)
Frequency of bending angles (%)
bending angle (degrees)
G
stimulated
dorsal
ventral
wild type
dve-1(uf171)
Frequency of bending angles (%)
bending angle (degrees)
H
Number of dorsal bends >50°
pre-stimulus
stimulus
pre-stimulus
stimulus
wild type
dve-1(uf171)
n=17
n=13
Average number of dorsal bends >50°
**
wild type
dve-1(uf171)

Figure 3: Failure of synapse elimination in *dve-1* mutants produces dorsal turning bias

(A) Scatter plot showing peak calcium response ($\Delta F/F_0$) in DD and VD GABAergic neurons to photostimulation of presynaptic DA and DB cholinergic neurons for wild type and *dve-1(uf171)* mutants. Horizontal bars indicate mean peak $\Delta F/F_0$ ± SEM. *** $p<0.001$, ANOVA with Tukey's multiple comparison. n=16; animals for each condition. Number of cells quantified: wt DD: 30, *dve-1(uf171)* DD: 27, wt VD: 64, *dve-1(uf171)* VD: 47.

(B) Representative locomotion tracks for wild type (black) and *dve-1(uf171)* (orange) animals recorded over 5 minutes of single worm tracking on NGM OP50 plates. Scale bar, 1 mm.

(C) Percentage of straight, curved, or circling tracks for wild type and *dve-1(uf171)* mutants.

(D) Tracks for wild type (left) and *dve-1* mutant (right) animals during forward runs (30 s) prior to or during photostimulation. Asterisks indicate start of track. D/V indicate dorsal and ventral directions.

(E) Schematics of bending angle measurements. Solid orange circles indicate the vertices (head, midbody, and tail) of the body bending angle (blue) measured.

(F) Frequency distribution of body bending angles measured prior to photosimulation for wild type (black) and *dve-1(uf171)* (blue). Negative bending angle values indicate dorsal, while positive bending angle values indicate ventral. Inset highlights bending events greater than 50°. wild type n=17, *dve-1(uf171)* n=13.

(G) Frequency distribution of body bending angles measured during photostimulation for wild type (black) and *dve-1(uf171)* (blue). Negative bending angle values indicate dorsal, while positive bending angle values indicate ventral. Inset highlights bending events greater than 50°. wild type n=17, *dve-1(uf171)* n=13.

(H) Left, scatterplot of total number of dorsal bends greater than 50° before and after photostimulation. Points with connecting line represents a single animal. Right, average number of dorsal bends greater than 50° during the period of photostimulation for wild type

and *dve-1(uf171)* animals. Bars indicate mean ± SEM. ***p*<0.01, student's t-test. wild type n=17, *dve-1(uf171)* n=13.

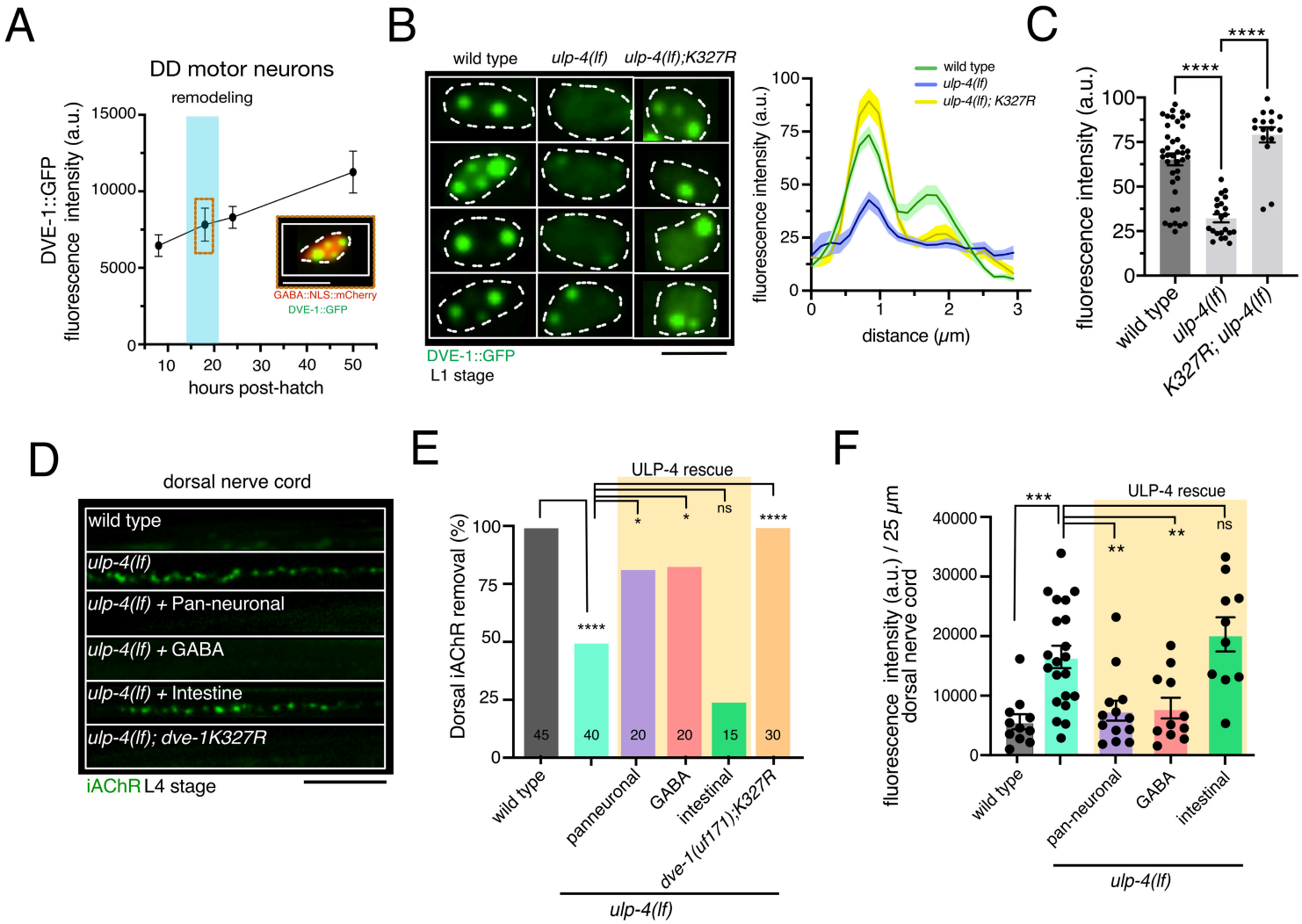
A
DD motor neurons
remodeling
DVE-1::GFP fluorescence intensity (a.u.)
15000
10000
5000
0
10
20
30
40
50
hours post-hatch
GABA::NLS::mCherry
DVE-1::GFP
B
wild type
ulp-4(lf)
ulp-4(lf);K327R
DVE-1::GFP
L1 stage
fluorescence intensity (a.u.)
100
75
50
25
0
0
1
2
3
distance (μm)
wild type
ulp-4(lf)
ulp-4(lf); K327R
C
fluorescence intensity (a.u.)
****
****
wild type
ulp-4(lf)
K327R; ulp-4(lf)
D
dorsal nerve cord
wild type
ulp-4(lf)
ulp-4(lf) + Pan-neuronal
ulp-4(lf) + GABA
ulp-4(lf) + Intestine
ulp-4(lf); dve-1K327R
iAChR L4 stage
E
ULP-4 rescue
Dorsal iAChR removal (%)
100
75
50
25
0
****
*
*
ns
****
45
40
20
20
15
30
wild type
panneuronal
GABA
intestinal
dve-1(uf171);K327R
ulp-4(lf)
F
ULP-4 rescue
fluorescence intensity (a.u.) / 25 μm dorsal nerve cord
40000
30000
20000
10000
0
***
**
**
ns
wild type
pan-neuronal
GABA
intestinal
ulp-4(lf)

Figure 4: DeSUMOylating peptidase ULP-4 regulates nuclear localization of DVE-1

(A) Fluorescence intensity of nuclear DVE-1::GFP in DD motor neurons at 10, 18, 22 and 50 hours after hatch. Nuclear DVE-1::GFP is organized in discrete foci and increases through development. Each time point indicates mean ± SEM from at least three independent experiments. Inset, representative image of nuclear DVE-1::GFP in DD motor neuron 18 hours after hatch (nucleus labeled by NLS::mCherry). White dashed line outlines nucleus. Scale bar, 3 μm.

(B) Confocal fluorescence images (left) of DVE-1::GFP in DD GABAergic motor neurons of L1 stage wild type, *ulp-4(lf)* mutant, and *K327R;ulp-4(lf)* double mutants. *ulp-4(lf)* disrupts DVE-1::GFP nuclear localization. DVE-1(K327R) disrupts SUMOylation of DVE-1 and restores DVE-1::GFP nuclear localization in *ulp-4(lf)*. White dashed line outlines nucleus. Scale bar, 3 μm. Right, line scan of nuclear DVE-1::GFP fluorescence intensity in DD motor neurons of wild type (green) n=16, *ulp-4(lf)* (blue) n=11 and DVE-1(K327R)*;ulp-4(lf)* double mutants (yellow) n=8. Solid line represents mean, shading represents standard deviation of fluorescence.

(C) Scatterplot (left) of the peak nuclear DVE-1::GFP fluorescence intensity in DD motor neurons. Each point represents a single DD nucleus. Imaged at least 2 DD cells per animal at L1 stage. Wild type: n=16, *ulp-4(lf)*: n=11, *K327R;ulp-4(lf)*: n=8. Bars indicate mean ± SEM. ****$p<0.0001$, ANOVA with Dunnett's multiple comparisons test.

(D) Fluorescent confocal images of iAChR clusters in the dorsal processes of L4 stage DD neurons. iAChRs remained present in the dorsal nerve cord of L4 stage *ulp-4(lf)* mutants, indicating a failure in juvenile synapse elimination. Either pan-neuronal or specific expression of wild type *ulp-4* cDNA in GABAergic neurons was sufficient to restore synapse elimination. Scale bar, 5 μm.

(E) Quantification of iAChR clustering at L4 stage for the genotypes indicated. Bars indicate the percentage of L4 stage animals where dorsal iAChRs have been completely removed. *$p<0.05$, ****$p<0.0001$, ns – not significant, Fischer's exact test with Bonferroni correction. 1/2 pan-neuronal lines, 2/2 GABA lines, and 0/2 intestinal rescue lines restored proper removal of dorsal iAChRs by L4.

(F) Scatterplot of average iAChR fluorescence intensity/25 μm in the dorsal nerve cord at L4 stage for the genotypes indicated. Each point represents a single animal. Bars indicate mean ± SEM. **$p<0.05$, ***$p<0.001$, ns – not significant, ANOVA with Dunnett's multiple comparisons test. The number of animals was >10 per genotype.

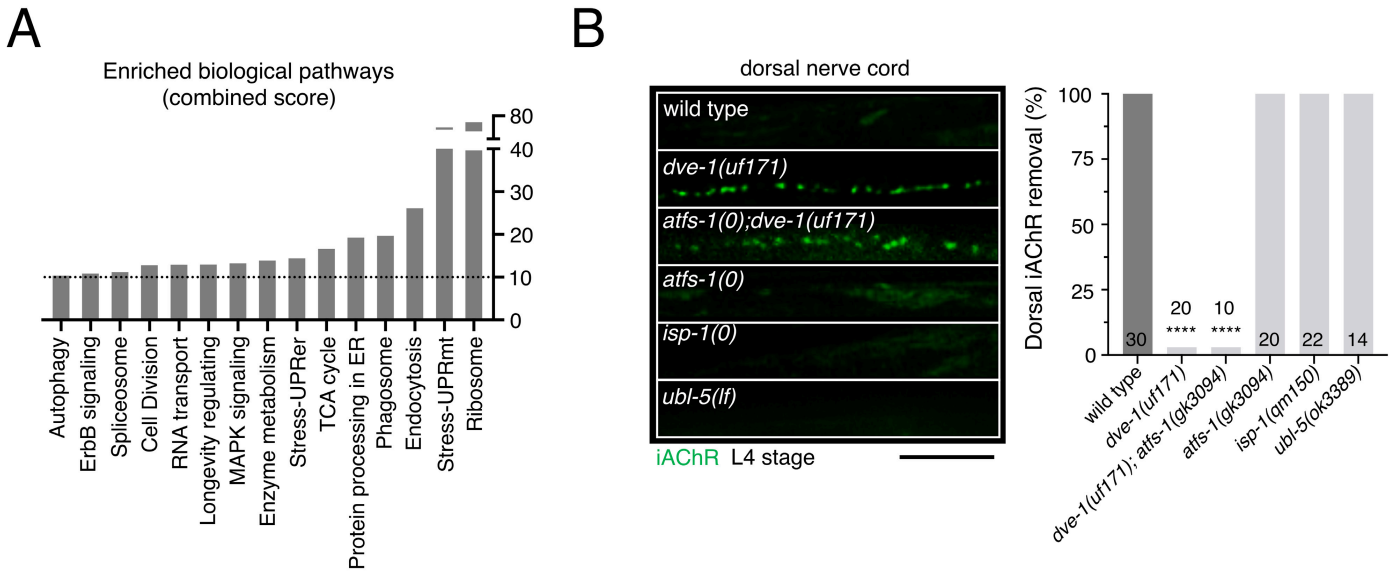
A
Enriched biological pathways
(combined score)
80
40
30
20
10
0
Autophagy
ErbB signaling
Spliceosome
Cell Division
RNA transport
Longevity regulating
MAPK signaling
Enzyme metabolism
Stress-UPRer
TCA cycle
Protein processing in ER
Phagosome
Endocytosis
Stress-UPRmt
Ribosome
B
dorsal nerve cord
wild type
dve-1(uf171)
atfs-1(0);dve-1(uf171)
atfs-1(0)
isp-1(0)
ubl-5(lf)
iAChR L4 stage
Dorsal iAChR removal (%)
100
75
50
25
0
30
20
****
10
****
20
22
14
wild type
dve-1(uf171)
dve-1(uf171); atfs-1(gk3094)
atfs-1(gk3094)
isp-1(qm150)
ubl-5(ok3389)

Figure 5 Enrichment analysis of DVE-1 ChIP-seq targets reveals potential pathways governing synapse elimination

(A) The WormEnrichR pathway enrichment analysis utilizing both the Kyoto Encyclopedia of Genes and Genomes (KEGG) database and the WikiPathway database. Bars represent enriched pathways with a combined score >10 (dashed line) and p-adj < 0.05. Y-axis is segmented between 40-60.

(B) Induction or inhibition of mtUPR has no effect on synapse elimination. Left, fluorescent confocal images of iAChR clusters in the dorsal processes of DD neurons at L4 stage. Scale bar, 5 μm. Right, bars indicate the percentage of L4 stage animals that have eliminated dorsal iAChRs. ****p< 0.0001, Fischer's exact test with Bonferroni correction.

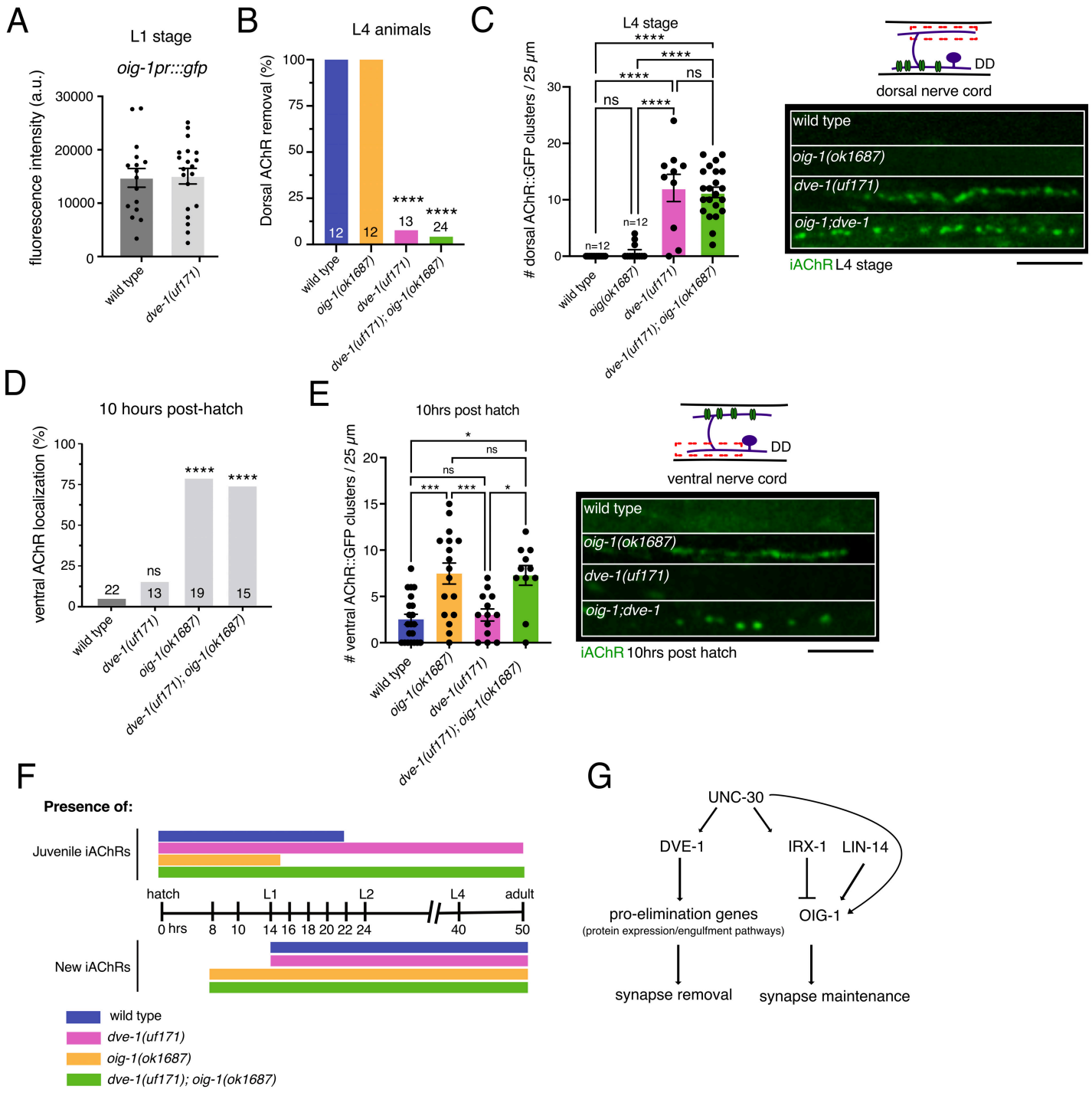
A
L1 stage
oig-1pr:::gfp
fluorescence intensity (a.u.)
30000
20000
10000
0
wild type
dve-1(uf171)
B
L4 animals
Dorsal AChR removal (%)
100
75
50
25
0
12
12
13
24
****
****
wild type
oig-1(ok1687)
dve-1(uf171)
dve-1(uf171); oig-1(ok1687)
C
L4 stage
dorsal AChR::GFP clusters / 25 µm
30
20
10
0
****
****
****
ns
ns
****
n=12
n=12
wild type
oig(ok1687)
dve-1(uf171)
dve-1(uf171); oig-1(ok1687)
DD
dorsal nerve cord
wild type
oig-1(ok1687)
dve-1(uf171)
oig-1;dve-1
iAChR L4 stage
D
10 hours post-hatch
ventral AChR localization (%)
100
75
50
25
0
22
ns
13
19
15
****
****
wild type
dve-1(uf171)
oig-1(ok1687)
dve-1(uf171); oig-1(ok1687)
E
10hrs post hatch
ventral AChR::GFP clusters / 25 µm
20
15
10
5
0
*
ns
ns
***
***
*
wild type
oig-1(ok1687)
dve-1(uf171)
dve-1(uf171); oig-1(ok1687)
DD
ventral nerve cord
wild type
oig-1(ok1687)
dve-1(uf171)
oig-1;dve-1
iAChR 10hrs post hatch
F
Presence of:
Juvenile iAChRs
hatch
L1
L2
L4
adult
0 hrs
8
10
14 16 18 20 22 24
40
50
New iAChRs
wild type
dve-1(uf171)
oig-1(ok1687)
dve-1(uf171); oig-1(ok1687)
G
UNC-30
DVE-1
IRX-1
LIN-14
pro-elimination genes
(protein expression/engulfment pathways)
OIG-1
synapse removal
synapse maintenance

Figure 6: *dve-1* synaptic destabilization acts parallel to *oig-1* antagonization of remodeling

(A) Average fluorescence intensity of *oig-1pr::gfp* in DD soma of L1 stage wild type and *dve-1* mutants. Each point represents a single DD cell body. Imaged 2 DD neurons/animal. Wild type n=8, *dve-1* mutants n=10. Bars indicate mean ± SEM.

(B) The percentage of animals where dorsal iAChRs are eliminated for L4 stage wild type, *oig-1(ok1687)*, *dve-1(uf171)* and *dve-1(uf171);oig-1(ok1687)* double mutants. ****$p<0.0001$, Fischer's exact test with Bonferroni Correction.

(C) Left, quantification of average number of iAChR clusters in L4 stage DD neurons per 25 µm of the dorsal nerve cord for the genotypes indicated. Each dot represents a single animal, at least 10 animals per genotype. Bars indicate mean ± SEM. ****$p<0.0001$, ns - not significant, ANOVA with Dunnett's multiple comparisons test. Right, fluorescent confocal images of iAChR clusters in L4 stage DD neurons of the dorsal nerve cord for the genotypes indicated. The precocious removal of dorsal iAChRs in *oig-1* mutants is reversed by mutation of *dve-1*. iAChR clusters persist through L4 stage in in both *dve-1* single and *oig-1;dve-1* double mutants. Scale bar, 5 µm.

(D) Quantification of iAChR ventral localization in DD neurons in wild type, *oig-1(ok1687)* mutant, *dve-1(uf171)* mutant and *dve-1(uf171), oig-1(ok1687)* double mutant L1 stage animals (10 hours). ****$p<0.0001$, ns-not significant, Fischer's exact test.

(E) Left, quantification of average number of iAChR clusters in DD neurons per 25 µm of the ventral nerve cord at L1 stage for the genotypes indicated. Each dot represents a single animal, at least 10 animals per genotype. Bars indicate mean ± SEM. ANOVA with Dunnett's multiple comparisons test, *$p<0.05$, ***$p<0.001$, ns-not significant. Right, fluorescent confocal images of iAChR clusters in the ventral processes of L1 stage DD neurons. Growth of ventral iAChR cluster occurs precociously in *oig-1* mutants and is unaffected by *dve-1* mutation. Scale bar, 5 µm.

(F) Timeline of development, approximate timing of transitions between larval stages and to adulthood are indicated. Bars indicate the presence of juvenile dorsal iAChRs (top) or ventral iAChRs formed during remodeling (bottom). *dve-1* mutants (magenta) fail to remove juvenile synapses but form ventral synapses normally. *oig-1* mutants (orange) show precocious removal of juvenile synapses and precocious formation of ventral synapses compared to wild type (blue). *oig-1;dve-1* double mutants (green) fail to remove juvenile synapses similar to *dve-1* single mutants, but show precocious formation of new ventral synapses similar to *oig-1* single mutants.

(G) Transcriptional control of DD remodeling. The GABAergic terminal selector transcription factor UNC-30/Pitx regulates the expression of both DVE-1 and OIG-1 (directly and indirectly) [28, 29], this paper. A second tier of transcriptional regulation by transcription factors LIN-14 and IRX-1 encodes temporal regulation of the Ig-domain protein OIG-1 [28, 29]. OIG-1 stabilizes juvenile synapses prior to remodeling. We show that DVE-1 promotes synapse removal/destabilization. Mutation of *dve-1* disrupts synapse removal, even in the absence of *oig-1*.

A

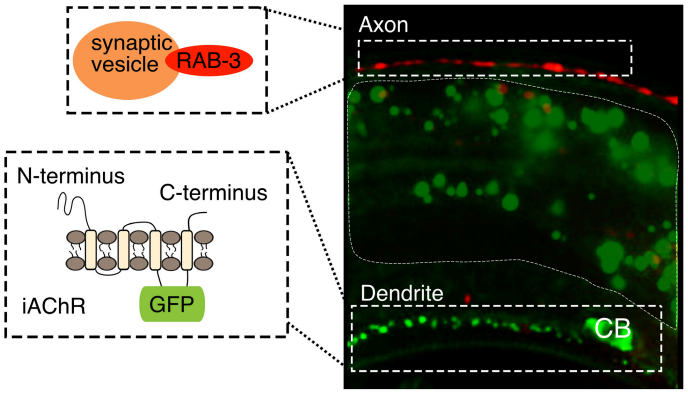
synaptic vesicle
RAB-3
N-terminus
C-terminus
iAChR
GFP
Axon
Dendrite
CB

B

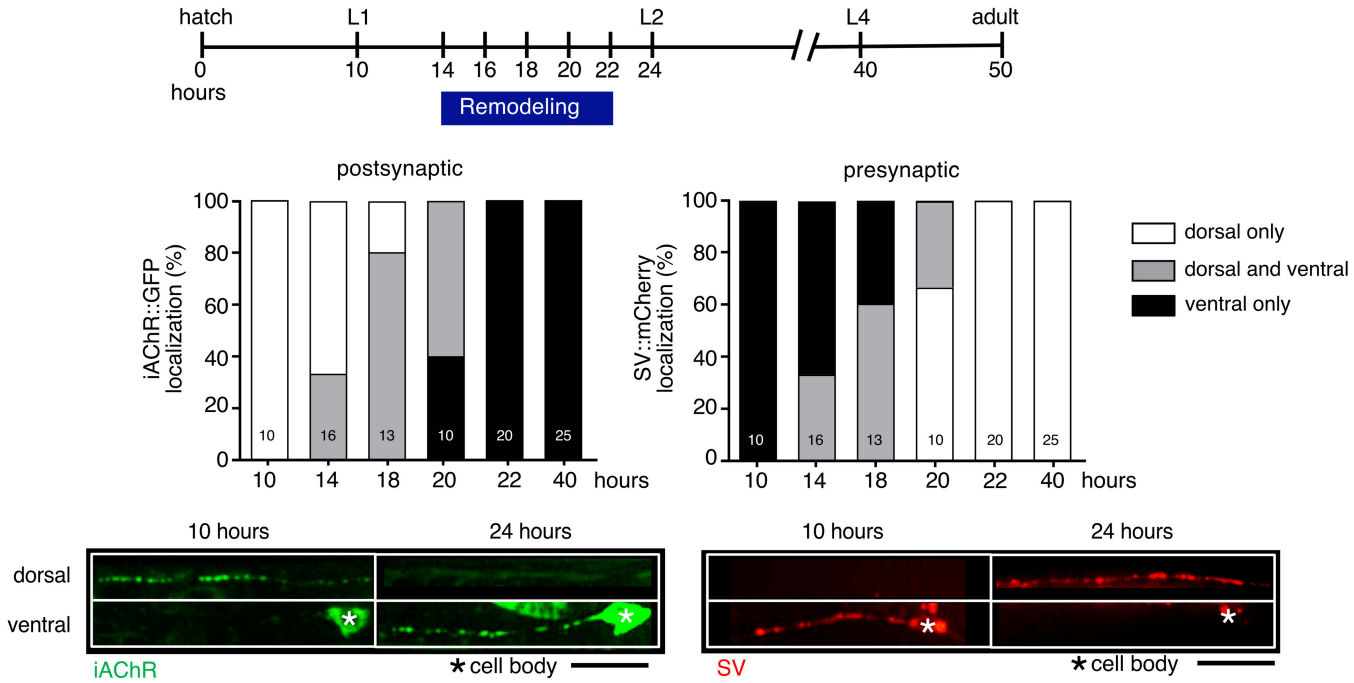
hatch
L1
L2
L4
adult
0
hours
10
14
16
18
20
22
24
40
50
Remodeling
postsynaptic
presynaptic
iAChR::GFP localization (%)
SV::mCherry localization (%)
100
80
60
40
20
0
10
14
18
20
22
40
hours
10
16
13
10
20
25
dorsal only
dorsal and ventral
ventral only
10 hours
24 hours
dorsal
ventral
iAChR
SV
* cell body

C

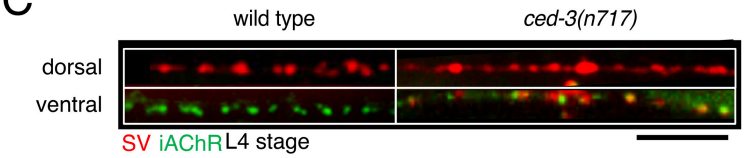
wild type
ced-3(n717)
dorsal
ventral
SV iAChR L4 stage

Supplemental Figures

Supplemental Figure 1.1: Remodeling of cholinergic postsynaptic sites and GABAergic presynaptic terminals occur simultaneously but are regulated by distinct mechanisms

(A) Confocal image L4 stage wild type animal co-expressing a synaptic vesicle marker, defined in inset as mCherry::RAB-3, and iAChR marker, defined in inset as ACR-12::GFP in DD neurons. Insets are schematic representations of each marker. Masking of intestinal autofluorescence is outlined by small white dotted line.

(B) Top, timeline of wild type development. Approximate timing of transitions between larval stages and to adulthood are indicated. Blue bar indicates duration of DD synaptic remodeling in wild type animals. Middle, quantification of iAChR (postsynaptic) remodeling (left) and SV (presynaptic) remodeling in DD neurons (right) at the indicated time points after hatch. Animals are binned as dorsal only (white), ventral only (black), or dorsal and ventral (grey) according to the distribution of iAChR (left) or SV (right) clusters. Bottom, representative images of dorsal and ventral iAChR clusters (left) and SV puncta (right) at the times indicated in DD neurons of wild type animals. Remodeling of iAChR clusters and SV puncta occur simultaneously. Scale bar, 5 μm.

(C) Merged confocal images showing SV puncta (red) and iAChR clusters (green) in dorsal and ventral DD neuron processes of wild type (left) and *ced-3(n717)* mutants (right). Scale bar, 5 μm.

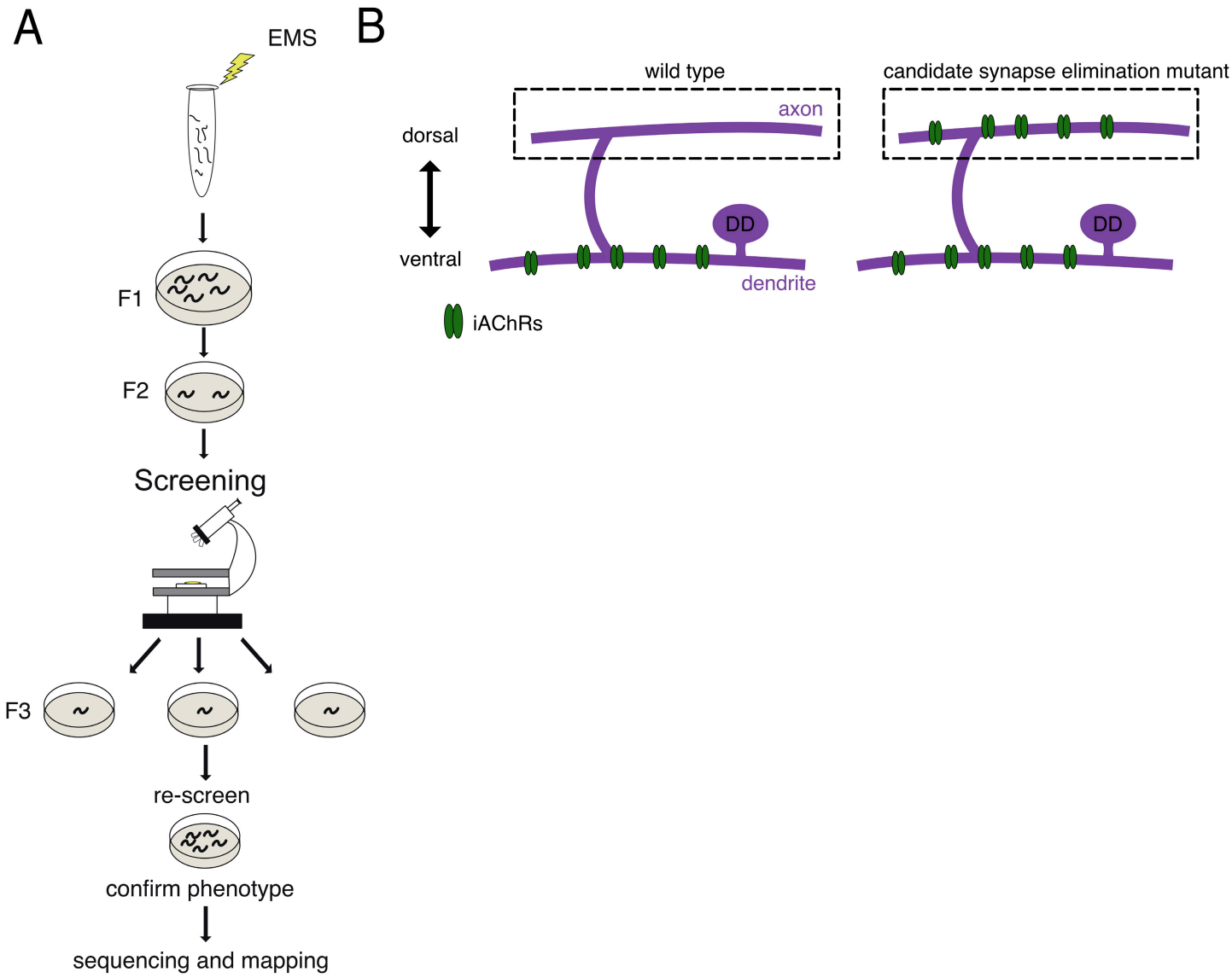
A
EMS
F1
F2
Screening
F3
re-screen
confirm phenotype
sequencing and mapping
B
wild type
candidate synapse elimination mutant
dorsal
ventral
axon
DD
dendrite
iAChRs

Supplemental Figure 1.2: A Forward genetic screen to identify conserved mechanisms controlling synapse elimination

(A) Schematic of experimental workflow for ethyl methanesulfonate (EMS) screen to obtain mutants with defects in the elimination of juvenile dorsal iAChR clusters.

(B) Schematics of iAChR localization within DD neurons of L4 stage wild type (left) or potential synapse elimination mutant (right).

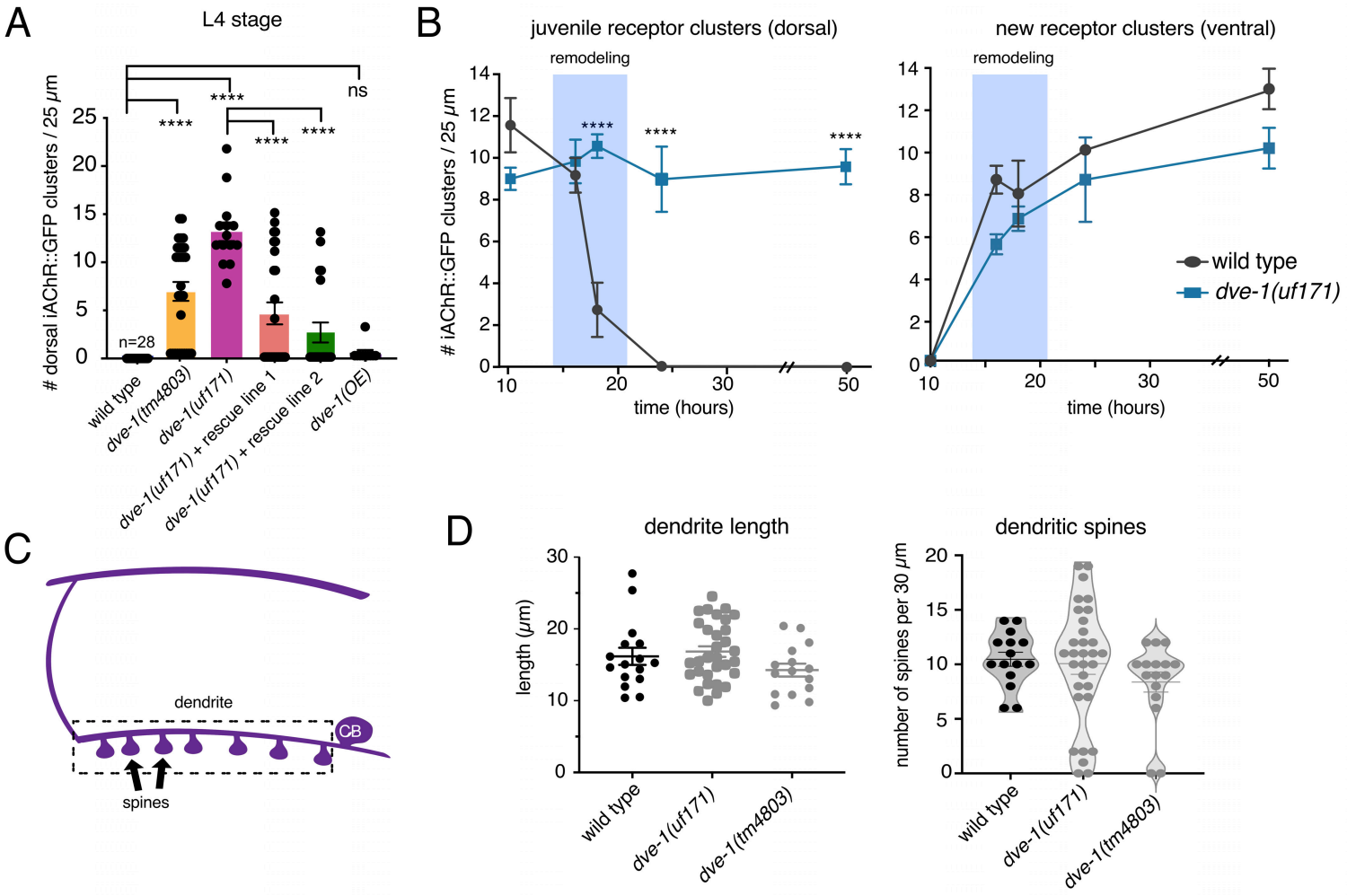
A
L4 stage
# dorsal iAChR::GFP clusters / 25 μm
n=28
****
****
****
****
ns
wild type
dve-1(tm4803)
dve-1(uf171)
dve-1(uf171) + rescue line 1
dve-1(uf171) + rescue line 2
dve-1(OE)
B
juvenile receptor clusters (dorsal)
new receptor clusters (ventral)
remodeling
iAChR::GFP clusters / 25 μm
time (hours)
wild type
dve-1(uf171)
C
dendrite
CB
spines
D
dendrite length
length (μm)
dendritic spines
number of spines per 30 μm
wild type
dve-1(uf171)
dve-1(tm4803)

Supplemental Figure 1.3: *dve-1* mutation disrupts synapse elimination but does not affect new synapse formation

(A) Quantification of average number of iAChR clusters per 25 µm in the dorsal nerve cord of L4 stage DD neurons for the genotypes. Bars indicate mean ± SEM. ****p<0.0001, ns - not significant, ANOVA with Dunnett's multiple comparisons test. Each point represents a single animal. The number of animals >10 per genotype.

(B) Average number of juvenile iAChR clusters in the dorsal nerve cord (left) and new iAChR clusters in the ventral nerve cord (right) at indicated times after hatch. iAChR clusters are removed from the dorsal nerve cord of wild type animals (black) during remodeling (blue shading) but persist in in the dorsal nerve cord of *dve-1* mutants (blue). iAChR clusters in the ventral nerve cords of wild type and *dve-1* mutants increase similarly over time. Data points indicate mean ± SEM. ****p<0.0001, student's t-test. The number of animals >10 per genotype.

(C) Schematic of DD neuron, segmented box represents area quantified in D. Arrows indicate dendritic spines, CB, cell body.

(D) Scatterplot of average length of DD neuron dendrite (left) and number of dendritic spines (right) in wild type (purple), *dve-1(uf171)* (dark blue), *dve-1(tm4803)* (teal) overlayed with a violin plot to show distribution. Each point represents a single animal. The number of animals >10 per genotype.

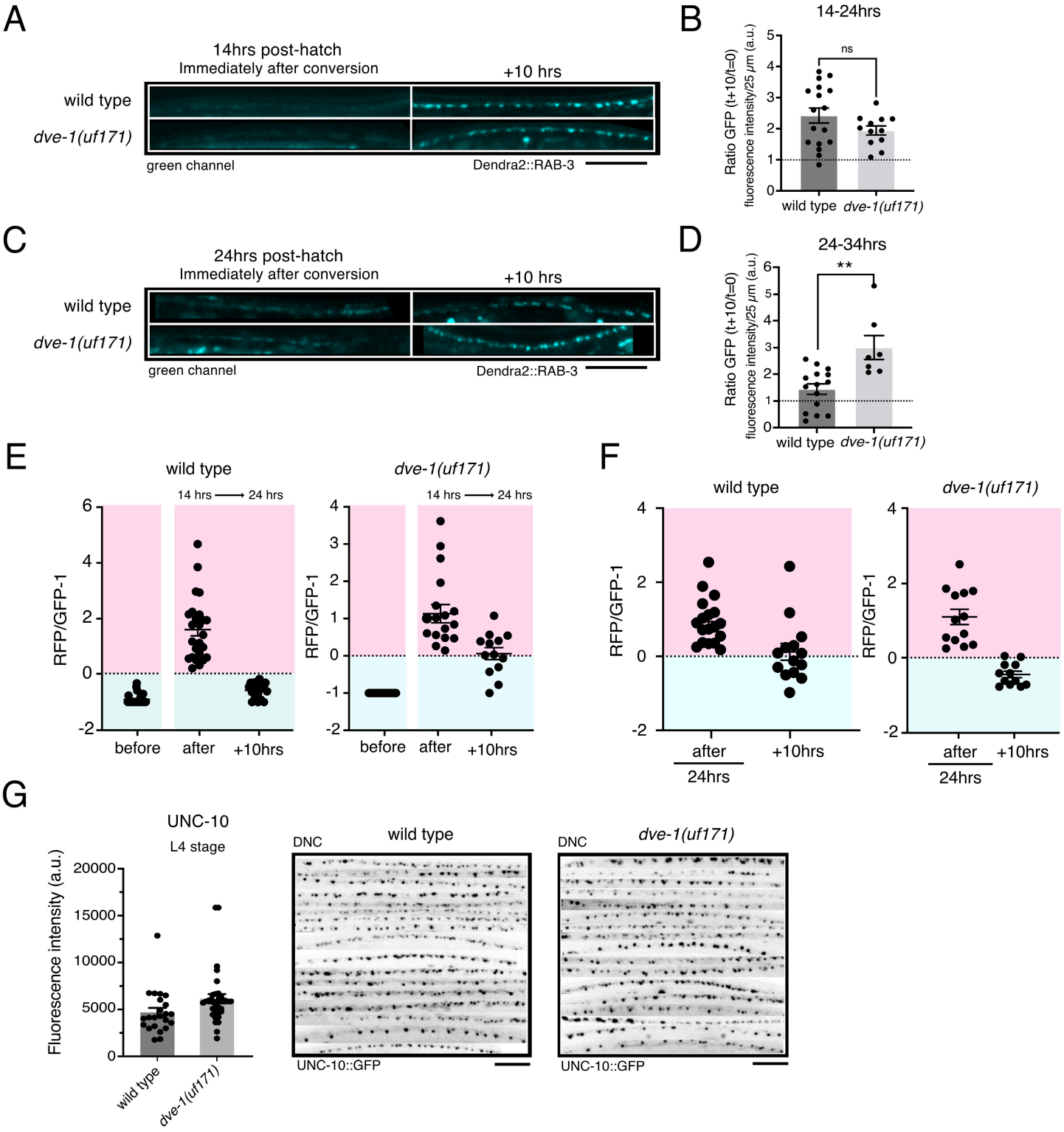
A
14hrs post-hatch
Immediately after conversion
+10 hrs
wild type
dve-1(uf171)
green channel
Dendra2::RAB-3
B
14-24hrs
ns
Ratio GFP (t+10/t=0)
fluorescence intensity/25 μm (a.u.)
wild type
dve-1(uf171)
C
24hrs post-hatch
Immediately after conversion
+10 hrs
wild type
dve-1(uf171)
green channel
Dendra2::RAB-3
D
24-34hrs
**
Ratio GFP (t+10/t=0)
fluorescence intensity/25 μm (a.u.)
wild type
dve-1(uf171)
E
wild type
dve-1(uf171)
14 hrs → 24 hrs
RFP/GFP-1
before
after
+10hrs
F
wild type
dve-1(uf171)
RFP/GFP-1
after
+10hrs
24hrs
G
UNC-10
L4 stage
Fluorescence intensity (a.u.)
wild type
dve-1(uf171)
DNC
wild type
UNC-10::GFP
DNC
dve-1(uf171)
UNC-10::GFP

Supplemental Figure 2.1: Presynaptic cholinergic synaptic vesicles turnover during remodeling

(A) Confocal images of the dorsal nerve cord of wild type (top) and *dve-1(uf171)* mutants (bottom) showing green Dendra2::RAB-3 clusters in cholinergic DA/B neurons either immediately after photoconversion from green to red at 14 hours after hatch (left) or 10 hours later (right). Similar amounts of green Dendra2::RAB-3 clusters are added during remodeling of wild type and *dve-1* mutants. Scale bar, 5 µm.

(B) Scatterplot showing green Dendra2::RAB-3 fluorescence intensity 10 hours after photoconversion normalized to fluorescence intensity immediately after photoconversion prior to remodeling (10 hours after hatch) for wild type (left) and *dve-1(uf171)* mutants (right). Each point indicates a single animal. The number of animals >10 per genotype. Bars indicate mean ± SEM. ns - not significant, student's t-test.

(C) Confocal images of the dorsal nerve cord of wild type (top) and *dve-1(uf171)* mutants (bottom) showing green Dendra2::RAB-3 clusters in cholinergic DA/B neurons either immediately after photoconversion from green to red at 24 hours after hatch (left) or 10 hours later (right). Similar amounts of green Dendra2::RAB-3 clusters are added during remodeling of wild type and *dve-1* mutants. Scale bar, 5 µm.

(D) Scatterplot showing green Dendra2::RAB-3 fluorescence intensity 10 hours after photoconversion normalized to fluorescence intensity immediately after photoconversion at 24 hours after hatch (after remodeling) for wild type (left) and *dve-1(uf171)* mutants (right). Each point indicates a single animal. The number of animals >6 per genotype. Bars indicate mean ± SEM. $^{**}p<0.01$, student's t-test.

(E) Scatterplots of Dendra2-RAB-3 RFP/GFP fluorescence intensity ratio measurements before photoconversion at 10 hours post hatch (before remodeling), immediately after, and 10 hours later for wild type and *dve-1* mutants. Expressed as RFP/GFP fluorescence ratio -1

for display purposes. Values less than zero indicate enhanced green fluorescence while values greater than 1 indicate enhanced red fluorescence. Each dot represents a single animal. The number of animals > 10 per genotype/timepoint.

(F) Scatterplots of Dendra2-RAB-3 RFP/GFP fluorescence intensity ratio measurements before photoconversion at 24 hours after hatch (after remodeling), immediately after, and 10 hours later for wild type and *dve-1* mutants. Expressed as RFP/GFP fluorescence ratio-1 for display purposes. Values less than zero indicate enhanced green fluorescence while values greater than 1 indicate enhanced red fluorescence. Each dot represents a single animal. The number of animals > 10 per genotype/timepoint.

(G) Left, scatterplot showing average UNC-10::GFP fluorescence intensity in L4 stage cholinergic neurons (*acr-5pr*::UNC-10::GFP) of the dorsal nerve cord (DNC) for wild type and *dve-1* mutants. Each point indicates a single animal, the number of animals >10 per genotype. Bars indicate mean ± SEM. Right, stacked fluorescent images of the dorsal nerve cord showing UNC-10::GFP clusters in cholinergic neurons of L4 stage wild type and *dve-1(uf171)* mutants. Images on each line are from different animals. Scale bar, 5 μm.

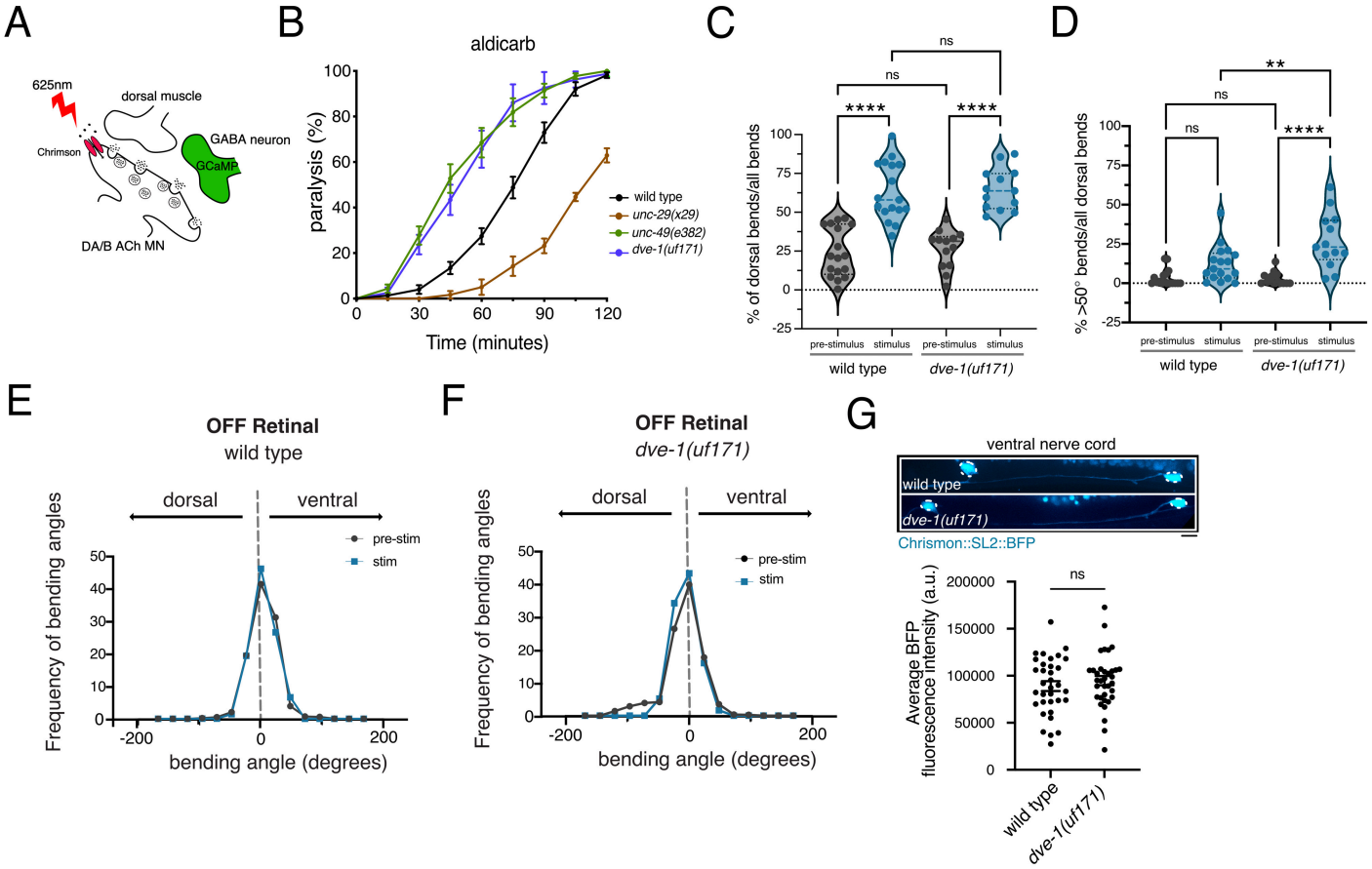
A
625nm
dorsal muscle
GABA neuron
Chrimson
GCaMP
DA/B ACh MN
B
aldicarb
paralysis (%)
Time (minutes)
wild type
unc-29(x29)
unc-49(e382)
dve-1(uf171)
C
% of dorsal bends/all bends
ns
****
pre-stimulus
stimulus
wild type
dve-1(uf171)
D
% >50° bends/all dorsal bends
**
ns
****
E
OFF Retinal
wild type
dorsal
ventral
pre-stim
stim
Frequency of bending angles
bending angle (degrees)
F
OFF Retinal
dve-1(uf171)
G
ventral nerve cord
wild type
dve-1(uf171)
Chrimson::SL2::BFP
Average BFP fluorescence intensity (a.u.)

Supplemental Figure 3.1: Circuit function is disrupted in DVE-1 mutants

(A) Schematic of combined cell-specific expression of Chrimson (red receptor) for cholinergic depolarization, and GCaMP6s monitoring [Ca^{2+}] changes in the post-synaptic GABAergic motor neurons (green).

(B) Time course of paralysis in the presence of aldicarb (1 mM) for wild type (black) (n=14), *unc-29(x29)* mutants (brown) (n=6), *unc-49(e382)* mutants (dark green) (n=16), *dve-1(uf171)* mutants (blue) (n=12), are shown. At least 10 animals per trial. Data represent mean ± SEM.

(C) Scatterplot with violin overlay of the percentage of dorsal bends for wild type and *dve-1(uf171)* mutants before and after photostimulation. Each point represents a single animal. The number of animals > 10 per genotype. ****p<0.0001, ns - not significant, ANOVA with Dunnett's multiple comparisons test.

(D) Scatterplot with violin overlay of the percentage of dorsal turns greater than 50° wild type (black) and *dve-1(uf171)* (blue) before and after photostimulation. Each point represents a single animal. The number of animals > 10 per genotype. **p<0.01, ****p<0.0001, ns - not significant, ANOVA with Dunnett's multiple comparisons test.

(E) Frequency distribution of body bending angles prior to (black) and during photostimulation (blue) for control animals in the absence of all-trans-retinal. Negative bending angle values indicate dorsal, while positive bending angle values indicate ventral. n=3.

(F) Frequency distribution of body bending angles prior to (black) and during photostimulation (blue) for *dve-1* mutants in the absence of all-trans-retinal. Negative bending angle values indicate dorsal, while positive bending angle values indicate ventral. n=3.

(G) Top, confocal images of DA/DB motor neurons from control and *dve-1* mutants expressing *punc-129::*Chrimson*::SL2::BFP*. Scale bar, 5 µm. Bottom, average fluorescence intensity of

DA/DB neuron cell bodies labeled by *punc-129::*Chrimson*::SL2::BFP*. Each dot represents a single DA/DB cell body, at least 15 animals per genotype were imaged.

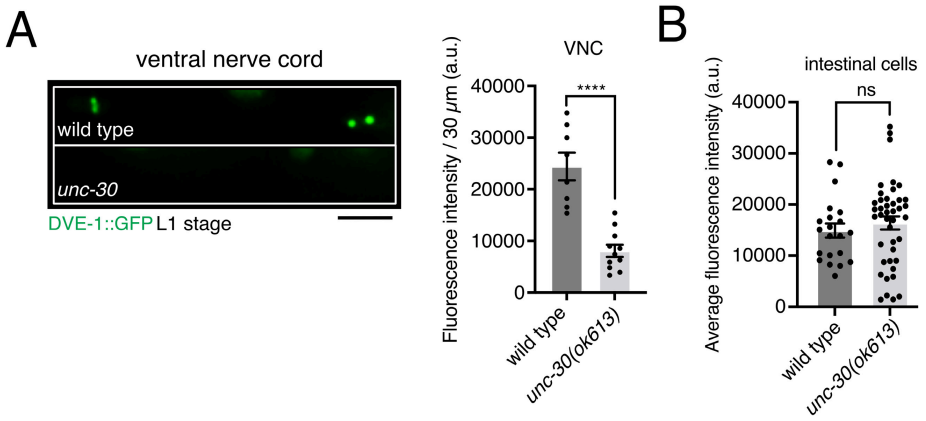
A
ventral nerve cord
wild type
unc-30
DVE-1::GFP L1 stage
VNC
Fluorescence intensity / 30 μm (a.u.)
40000
30000
20000
10000
0
****
wild type
unc-30(ok613)
B
intestinal cells
Average fluorescence intensity (a.u.)
40000
30000
20000
10000
0
ns
wild type
unc-30(ok613)

Supplemental Figure 4.1 The Pitx/UNC-30 transcription factor regulates expression of DVE-1 in GABAergic neurons

A. Top, confocal fluorescence images of ventral nerve cord expression of DVE-1::GFP in DD GABAergic motor neurons of L1 stage wild type and *unc-30(ok613)* mutants. Scale bar, 5 µm. Bottom, scatterplot of average fluorescence intensity measures of ventral nerve cord (VNC) 30 µm ROI. Each dot represents a single animal. wild type n=8, *unc-30(ok613)* n=11. Bars indicate mean ± SEM. ****p<.0001, student's t-test.

B. Scatterplot of average nuclear DVE-1::GFP fluorescence intensity in intestinal cells of L1 stage wild type and *unc-30(ok613)* mutants. Each point represents a single intestinal cell. Imaged 3 intestinal cells per animal. Wild type n=8, *unc-30* mutants n=11. Bars indicate mean ± SEM. ns - not significant, student's t-test.

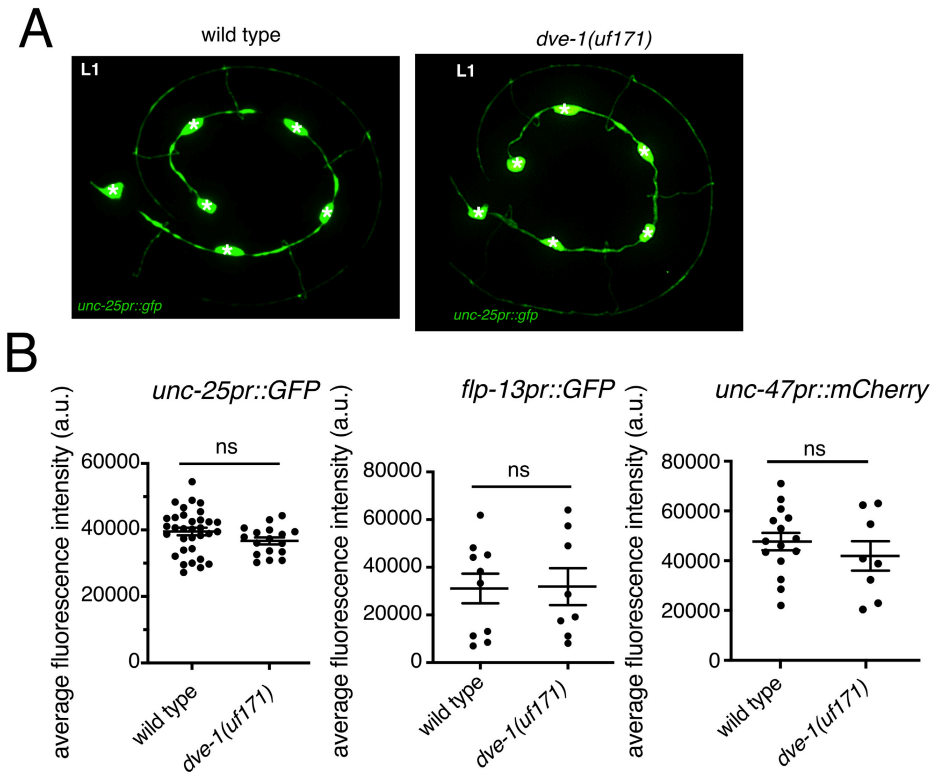
A
wild type
dve-1(uf171)
L1
L1
unc-25pr::gfp
unc-25pr::gfp
B
unc-25pr::GFP
flp-13pr::GFP
unc-47pr::mCherry
average fluorescence intensity (a.u.)
ns
60000
40000
20000
0
80000
wild type
dve-1(uf171)

Supplemental Figure 5.1: Homeodomain TF DVE-1 does not affect development of GABAergic motor neurons

(A) Representative image of wild type (right) and *dve-1(uf171)* mutant (left) animals labeling DD neurons with *punc-25::GFP* at the L1 developmental stage. *-Cell body.

(B) Average fluorescence intensity of DD1, DD2, and DD3 neuron cell bodies in three distinct GABA reporter backgrounds, *unc-47pr::mCherry,* and *unc-25pr::GFP, flp-13pr::GFP* in wild type and *dve-1(uf171)* mutants at the L1 developmental stage. Each dot represents a single cell body, at least 8 animals per genotype. Bars indicate mean ± SEM. ns-not significant, students t-test.

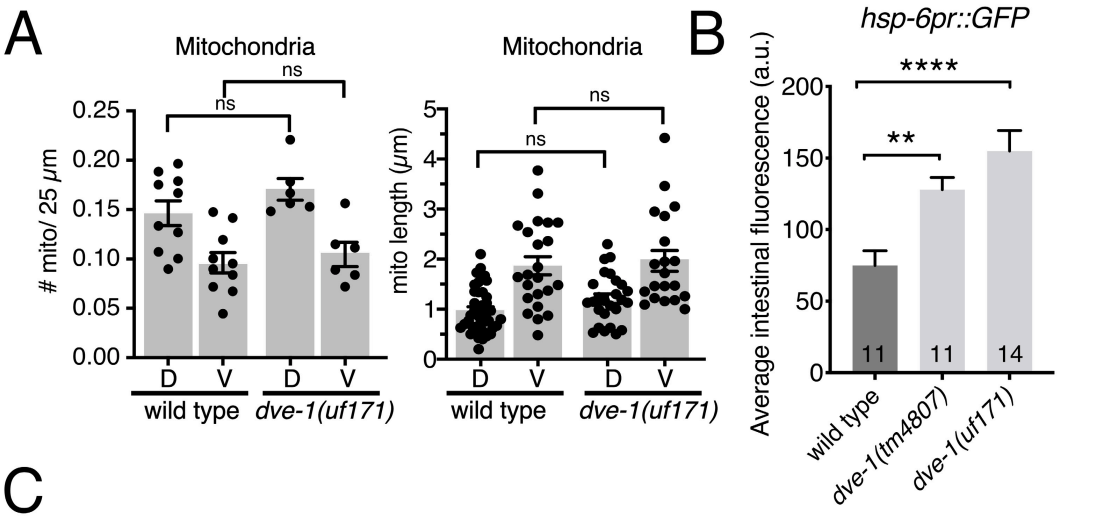
A
Mitochondria
ns
ns
mito/ 25 μm
0.25
0.20
0.15
0.10
0.05
0.00
D V D V
wild type dve-1(uf171)
Mitochondria
ns
ns
mito length (μm)
5
4
3
2
1
0
D V D V
wild type dve-1(uf171)
B
hsp-6pr::GFP
****
**
Average intestinal fluorescence (a.u.)
200
150
100
50
0
11 11 14
wild type
dve-1(tm4807)
dve-1(uf171)

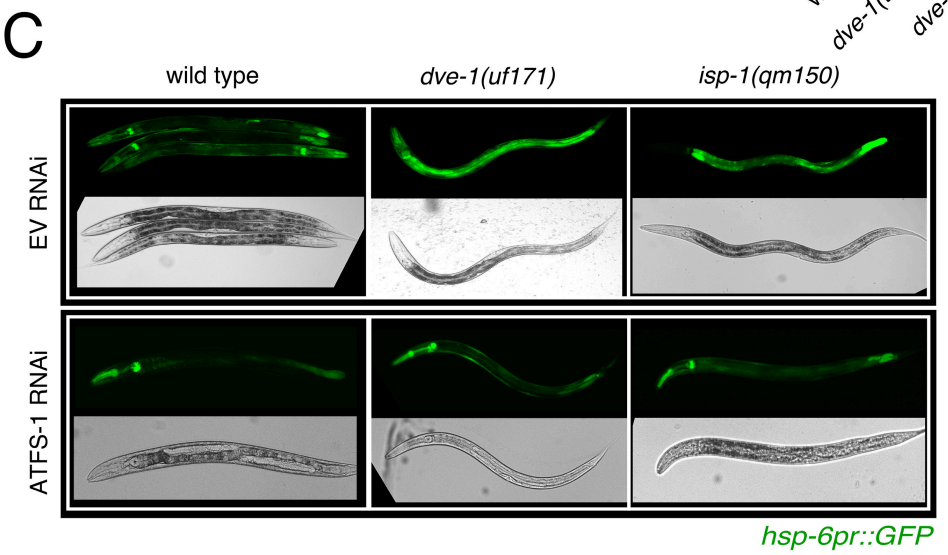
C
wild type
dve-1(uf171)
isp-1(qm150)
EV RNAi
ATFS-1 RNAi
hsp-6pr::GFP

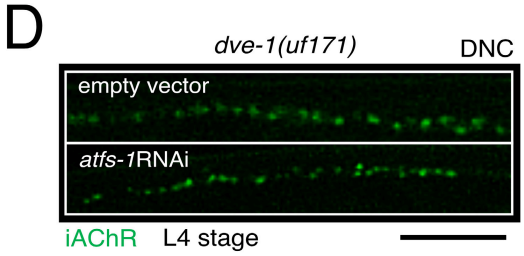
D
dve-1(uf171)
DNC
empty vector
atfs-1RNAi
iAChR
L4 stage

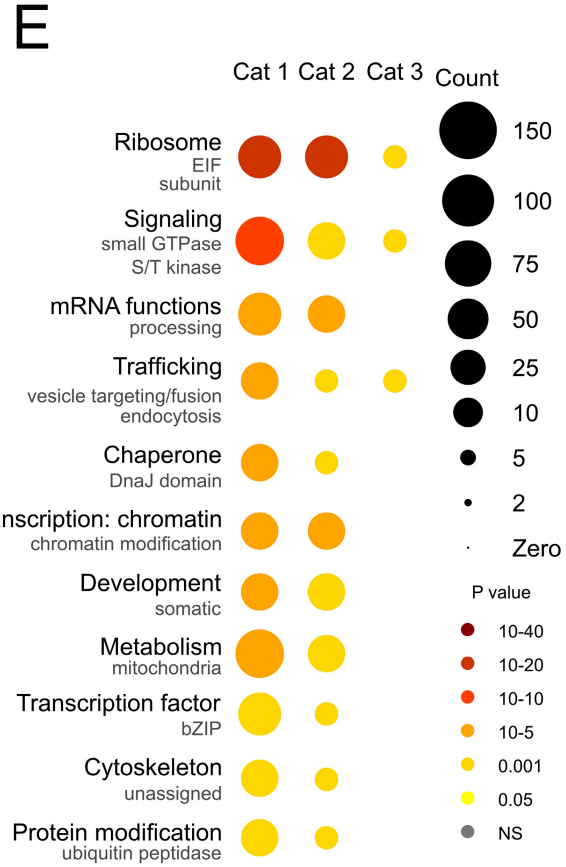
E
Cat 1 Cat 2 Cat 3
Count
Ribosome
EIF subunit
Signaling
small GTPase
S/T kinase
mRNA functions
processing
Trafficking
vesicle targeting/fusion
endocytosis
Chaperone
DnaJ domain
Transcription: chromatin
chromatin modification
Development
somatic
Metabolism
mitochondria
Transcription factor
bZIP
Cytoskeleton
unassigned
Protein modification
ubiquitin peptidase
150
100
75
50
25
10
5
2
Zero
P value
10-40
10-20
10-10
10-5
0.001
0.05
NS

Supplemental Figure 5.2: Removal of iAChRs in GABA MNs is not disrupted by either activation or inhibition of the mtUPR

(A) Left, scatterplot of mitochondrial density (number of mitochondria/25 μm) in dorsal (D) and ventral (V) processes of DD neurons of L4 stage wild type and *dve-1(uf171)* mutants. Each point represents a single animal, wild type n=10, dve-1(uf171) n=6. Right, average length of mitochondria in dorsal and ventral processes of DD neurons of L4 stage wild type and *dve-1(uf171)* mutants. Each dot represents a single mitochondria, wild type n=10, *dve-1(uf171)* n=6. Bars indicate mean ± SEM, ANOVA with Dunnett's multiple comparisons test. ns- not significant.

(B) Average fluorescence intensity measures of intestinal ROI in wild type, dve-1(tm4807), and dve-1(uf171) animals expressing *hsp-6pr::GFP* transgene. Bars represent mean ± SEM. ANOVA with Dunnett's multiple comparisons test. ** $p < 0.01$, **** $p < 0.0001$.

(C) Fluorescent images of transgenic worms expressing the mtUPR reporter *hsp-6pr::*GFP and treated with either empty vector (top) or RNAi targeting *atfs-1* (bottom). *dve-1(uf171)* mutants show increased expression of *hsp-6pr::*GFP under basal conditions compared with control animals and this is reversed by RNAi targeting *atfs-1*. *isp-1* mutants also have elevated mtUPR and are included as a control.

(D) Fluorescent confocal images of iAChR clusters in dorsal nerve cord (DNC) of DD neurons of L4 stage *dve-1(uf171)* mutants treated with either empty vector or RNAi targeting *atfs-1*. *atfs-1* RNAi reverses the elevated mtUPR of *dve-1* mutants but does not normalize synapse elimination. Scale bar, 5 μm.

(E) Wormcat analysis for significantly enriched categories of putative DVE-1 targets identified from ChIP-seq dataset. size of circles indicates the number of genes and color indicates the value of significant over-representation in each Wormcat category.